2D magneto-optical trap as source for cold ions

Kusters, D.J.N.

Award date:
2008

CONFIDENTIAL REPORT

2D Magneto-Optical Trap as Source for Cold Ions

D.J.N. Kusters

October 21, 2008
Eindhoven, University of Technology

CQT 2008 - 14

Supervisors:
dr.ir. E.J.D. Vredenbregt
ir. M.P. Reijnders

Committee:
dr.ir. E.J.D. Vredenbregt
ir. M.P. Reijnders
prof.dr.ir. G.M.W. Kroesen
dr.ir. R.R. Trieling
dr.ir. O.J. Luiten

Eindhoven, University of Technology
Department of Applied Physics
Coherence & Quantum Technology
Den Dolech 2
5600 MB Eindhoven
The Netherlands

"I have no special talents. I am only passionately curious."

Albert Einstein

This report is **CONFIDENTIAL** due to a patent application concerning the work presented in Chapter 6

Abstract

High brightness electron and ion beams find many applications in science and technology. In particular, ion beams are widely used by the semiconductor industry as high precision milling tools in so-called Focused Ion Beams (FIB). Due to the continuing demand to reduce the size of typical structures on semiconductor wafers, there is a need to improve the properties, such as the brightness, of ion sources.
A new technique to produce electron and ion beams from ultra-cold plasmas has been developed recently. Such a plasma is created by near-threshold photo-ionization of a cloud of laser-cooled atoms that are trapped in a so-called Magneto-Optical Trap (MOT).
In this thesis we present two related but separated investigations that aim to improve the properties of such a laser-cooled source.
In the first part we improve an existing setup by adding an atomic beam source from which the MOT can be loaded. We experimentally investigate the conditions that optimize the source flux. We were able to increase the rate at which atoms are loaded into the trap by a factor of 10, to 5×10^8 atoms/s. At the same time the trapping lifetime increased by a factor of 3, to 10 seconds. These improvements enables higher source brightness and extraction current.
In the second part a new type of compact ultra-cold Rb^+ ion source is proposed and its properties are investigated through numerical simulations. The source consists of an atomic beam extracted from a Knudsen-cell, which is then transversely cooled and compressed using a Magneto-Optical Compressor (MOC). We studied the performance of the source as function of several laser cooling parameters and find that we can obtain a reduced peak brightness of 4×10^8 A/sr m^2 V at a current of 1.5 nA for a source temperature of 100^oC. This new type of ion source can also be used with a light ions such as lithium for high resolution ion microscopy or with heavy ions as cesium for Time-of-Flight Secondary Ion Mass Spectroscopy (ToF-SIMS).

Contents

Chapter 1

Introduction

1.1 The Ultra Cold Plasma project

Bright electron bunches and ion beams are used in many areas of science and technology. For instance, bright electron bunches can be used to observe very fast structural changes in femtosecond chemistry [1] and are needed for the operations of a free electron laser [2]. Focused ion beams (FIB), on the other hand, find applications in semiconductor industry for high precision milling and deposition, enabling device modification, mask repair and failure analysis [3].

The brightness B of a source is defined as the current density per unit of solid angle and per unit of energy spread [4]. Today state-of-the-art electron bunches are produced by a radio-frequency photogun [5]. New developments showed that the brightness can be increased by maximizing the current density by minimizing the source area. However, such photo-emitters produces electrons with temperatures of about 5000 K. It can be shown that the brightness B scales inversely proportional to the initial temperature ($B \propto T^{-1}$) [6]. In this Ultra Cold Plasma (UCP) project our strategy is to obtain bright electron and ion beams by starting from an ultra cold plasma as a source for the electrons and ions. In this way a plasma with initial electron temperatures around 10 K can be obtained. This is 2 - 3 orders of magnitude lower than the photo-emitter sources. By using a low temperature instead of a small area, we are able to achieve a high brightness, generating less space charge effects that play an important role in the current Liquid Metal Ion (LMI) sources [7].

The basic idea for the production of ultra cold electron bunches in the UCP project is shown in Figure 1.1. First we start by creating a cold ($T < 1$ mK) cloud of atoms trapped in a Magneto-Optical Trap (MOT) in a volume of a few mm^3 with densities up to 10^{18} m^{-3}. From this cold cloud of atoms a fraction is excited to an intermediate state using a quasi-continuous μs laser pulse ($\lambda = 780$ nm in case we use Rb). Then a laser ($\lambda = 480$ nm again for Rb) ionizes the excited atoms within the volume irradiated by both lasers. Here a UCP with a charge up to 100 pC is created. The electrons within this UCP will be heated up to $\approx$10 K due to ns-timescale heating processes [6]. Finally bunches are extracted by applying an electric field over the UCP cloud. The

aim is to apply a 1 MV voltage across a 1 cm gap, which is switched extreme rapidly (<1 ns) to prevent space charge induced emittance[1] growth during acceleration. The same principle can be used to create continuous or pulsed ion beams/bunches. The research done during this master thesis served the goals of the UCP project towards the realization of state-of-the-art electron and ion beams/bunches. Which part of the research is covered in this thesis will be explained in the next section.

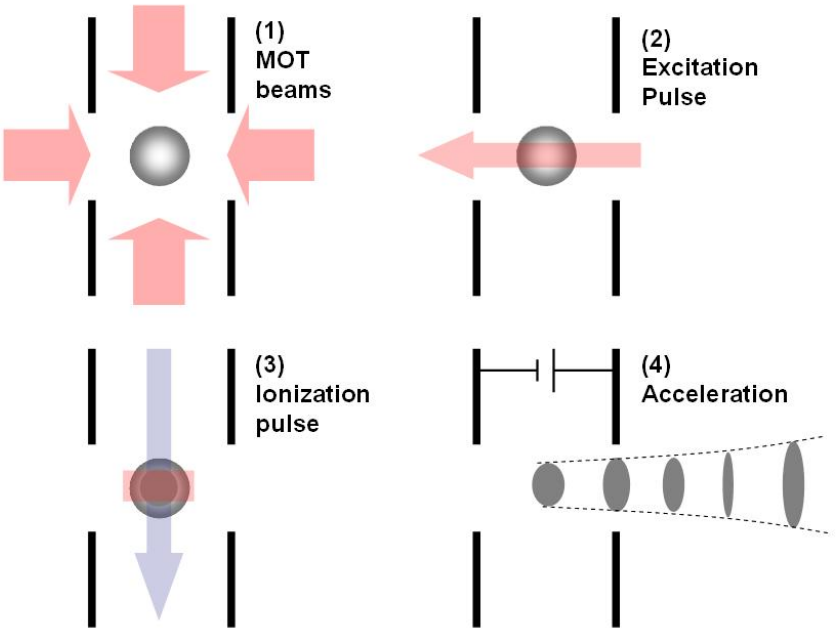

Figure 1.1: *Schematic overview of the four step procedure to realize a Ultra Cold Plasma (UCP) electron source.*

1.2 This thesis

This thesis is composed out of two parts. In the first part a study is done to optimize the loading rate and lifetime of the three-dimensional Magneto-Optical Trap (3D-MOT) by using a two-dimensional Magneto-Optical Trap (2D-MOT) as a source of slow atoms. To produce very bright electron bunches and ion beams from an ultra cold plasma, the loading rate and lifetime of this atomic cloud have to be optimized. Currently, the atomic cloud (3D-MOT) is loaded from a background rubidium vapor which limits the loading rate, and due to background gas collisions the lifetime is very short (2-3 s). In this work a cold atomic beam from a 2D-MOT is used to load the 3D-MOT in order to increase the loading rate and lifetime of the atomic cloud.
In Chapter 2 we will start with an introduction about laser cooling and trapping. Here

[1] The emittance ϵ is a Lorentz-invariant measure for the focusability of a particle beam [6]. Brightness is inversely proportional to ϵ^2.

the theoretical basis of this work is explained. The experimental setup for the atomic beam source, i.e. the 2D-MOT, used in this project is based on the work of Dieckmann *et al.* [13] and Schoser *et al.* [14]. In Chapter 3 we present an overview of both articles as well a model for our 2D-MOT as source for the 3D-MOT. Chapter 4 gives an overview of the experimental setup and finally in Chapter 5 the experimental results are presented together with the necessary discussion.

The second part starts in Chapter 6, where a new type of compact ultra-cold Rb^+ ion source is presented. The concept is based on the ionization of cold atoms from a laser cooled atomic beam as proposed by Freinkman *et al* [8]. With a rubidium vapor cell oven, a so-called Knudsen cell, as a source, an atomic beam is created. This atomic beam is cooled and compressed using a Magneto-Optical Compressor (MOC) to a beam with a diameter around 100 μm and transverse temperature in the order of 200 μK. In the the following sections the basic concept of this new source is presented together with an estimate of performance. This estimate shows very promising numbers for the brightness and current of the source, exceeding state-of-the-art technologies. To study the performance of this new type of ion source more in detail, numerical simulations has been done to calculate the properties of an atomic beam after passing through a MOC. The results of these simulations are presented followed by a suggestion for some potential ion beam applications. We will end this thesis by summarizing the conclusions of both parts together with the outlook.

Chapter 2

Laser Cooling and Trapping

Laser cooling and trapping of neutral atoms is a rapidly expanding area of physics research and has seen a lot of developments over the last decade. In this chapter we will introduce some basics of laser cooling and trapping. This theory is important to understand the measurements, simulations and modeling in the rest of this thesis.
We will start to introduce the most important concepts by starting with the Doppler effect. Step by step we will expand the theory until a basic overview is given. A more detailed and comprehensive description can be found in the books by Metcalf and Van der Straten [11] or Foot [10].

2.1 The Doppler effect

Atoms traveling with a certain velocity $\vec{v}$ through a laser beam with frequency ω_L and wavevector $\vec{k}$, will observe a different laser frequency ω_D. This phenomenon is called the Doppler effect and is quantified by

$$\omega_D = \omega_L - \overrightarrow{k} \cdot \overrightarrow{v}. \tag{2.1}$$

It is the component of the velocity along $\overrightarrow{k}$ that leads to the Doppler effect. In Figure 2.1 an example is given. Here an atom is moving with velocity v along the x-axis. Photons with frequency ω_L are traveling from both directions along the x-axis. For a simple 2-level atom, a photon will be absorbed if the photon's frequency is resonant with the atom's frequency. This will occur if the difference in frequency between the laser and the atom, which we will call the detuning δ, equals

$$\delta = \omega_L - \omega_0 = \overrightarrow{k} \cdot \overrightarrow{v}, \tag{2.2}$$

where ω_0 is the atom's frequency. The absorbtion probability is characterized by the line shape function[1] $g(\omega)$ given by

$$g(\omega) = \frac{1}{2\pi} \frac{\Gamma}{(\omega - \omega_0)^2 + \Gamma^2/4}, \tag{2.3}$$

which has a Lorentzian shape centered around ω_0, and where Γ is the natural line width of the atom. This Doppler effect is the basic mechanism behind optical molasses, i.e. Doppler cooling. We will introduce the optical molasses technique in the next section.

[1] The area under the line shape function equals unity: $\int_{-\infty}^{\infty} g(\omega) d\omega = 1$.

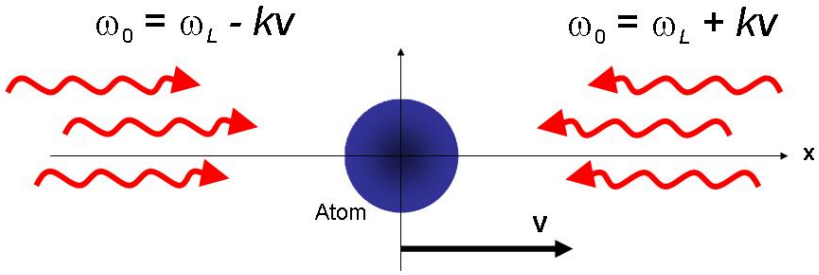

Figure 2.1: *Due to the Doppler effect the photons with frequency ω_L coming from the left will be observed by the atoms as photons with frequency $\omega_L - kv$ and those coming from the right with $\omega_L + kv$.*

2.2 The Optical Molasses technique

In the previous section we learned that if laser light becomes close to resonance with the atoms, satisfying Equation 2.2 and Equation 2.3, the photons can be absorbed by the atom. A photon has an energy $E_\gamma = \hbar\omega_L$ and momentum $p_\gamma = \hbar k$. Due to the conservation of momentum the atom will experience a momentum change when it absorbs a photon. In Figure 2.2 we see an atom moving towards a laser beam. Each time a photon is absorbed, the atom experiences a momentum kick from the photon opposite to its motion. The scattered photons are emitted in a random direction and deliver no net force. The sum of all the momentum kicks results in a force that slows the atom. This force is called the scattering force and is proportional to the rate of change in momentum $F = \hbar k \times R$. The scattering rate R, which has a Lorenzian shape, is given by

$$R = \frac{\Gamma}{2}\frac{s_0}{1 + s_0 + 4\delta^2/\Gamma^2}, \tag{2.4}$$

where $s_0 = I/I_0$ is the saturation parameter giving the ratio between the laser intensity I and saturation intensity I_0, which is an atomic property. The scattering of many photons lead to a net force

$$F = \hbar k \times \frac{\Gamma}{2}\frac{s_0}{1 + s_0 + 4\delta^2/\Gamma^2}. \tag{2.5}$$

For small values of s_0 this force is linear with laser intensity.

With one laser beam, deceleration of an atomic beam can be accomplished. If we apply two counter propagating laser beams with the same laser detuning δ, we are able to decelerate the atoms in the corresponding dimension. This is illustrated in Figure 2.3. Once the atoms are at rest, the forces balance each other out and the atoms remain at rest. We now have "cooled" the atoms in one dimension.

This cooling force is called the optical molasses force. Mathematically the force ex-

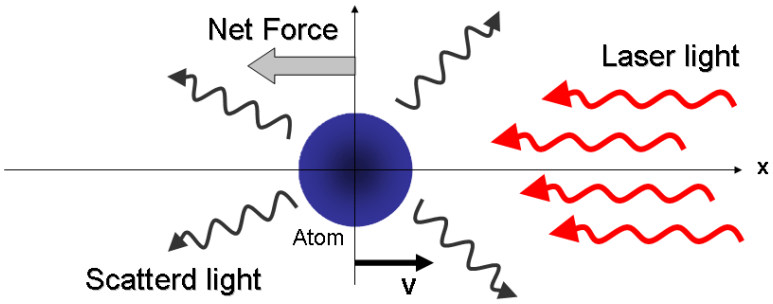

Figure 2.2: *For an atom moving towards a laser, each absorbed photon gives the atom a momentum kick in the direction opposite to its motion. The scattered photons are emitted in a random direction and delivers no net force. The sum of the momentum kick's results in a force that slows the atom.*

perienced by two counter propagating laser beam is given by

$$F_{\text{molasses}} = -\hbar k \frac{\Gamma}{2}\left[\frac{-s_0}{1+s_0+\left[\frac{2(\delta+kv)}{\Gamma}\right]^2} + \frac{s_0}{1+s_0+\left[\frac{2(\delta-kv)}{\Gamma}\right]^2}\right]. \tag{2.6}$$

For small values of v this force is proportional and opposite to the atoms velocity, and with $\delta < 0$, the force can be approximated by

$$F_{\text{molasses}} \approx -\alpha v, \tag{2.7}$$

where α is the damping coefficient given by

$$\alpha = \hbar k^2 s_0 \frac{-2\delta/\Gamma}{[1+s_0+(2\delta/\Gamma)^2]^2}. \tag{2.8}$$

Again, Equation 2.7 is only valid for small laser intensities ($s_0 \ll 1$).

The solution of Equation 2.7, given an initial velocity v_0, is

$$v(t) = v_0 e^{-\frac{\alpha}{m}t}, \tag{2.9}$$

which gives the evolution of the atom's velocity over time. This solution is only valid if $v_0 \ll v_{cap}$. Here v_{cap} is the capture velocity, defined as the velocity for atoms where the molasses force is maximal. This capture velocity is approximately $\pm\delta/k$.

Unfortunately, the final temperature of atoms that can be obtained with the optical molasses technique is limited. When a photon is absorbed by an atom moving in the opposite direction, its velocity is decreased due to momentum conservation. So when a photon is emitted by this excited atom, there is an extra momentum added to the atom. Since emission is in a random direction, this effect averages out, and on a time average, there is just a little increase in the atom's momentum due to emission. At the temperature where this effect exactly balances out the cooling effect of the laser,

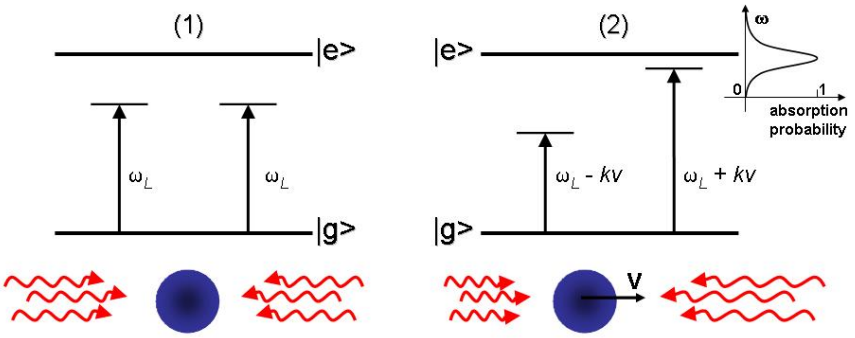

Figure 2.3: *In (1) the atom is at rest and experiences no net force. In (2) the atom is moving with velocity v and due to the Doppler effect the atom will experience a net force opposite to its velocity that will result in a deceleration. This force originates from the right laser beam that is detuned in resonance with the atom by the Doppler shift. In the right upper corner the Lorentzian shaped absorbtion probability is shown.*

no further Doppler cooling is possible. So when this occurs there is an equilibrium between the cooling process due to the optical molasses force ($\frac{1}{2}m\frac{d}{dt}v^2 = -\alpha v$) and the heating process due to the random scattering ($\frac{1}{2}m\frac{d}{dt}v^2 = 2\eta E_r R$, where $\eta = 1/3$ [10] is the angular average for isotropic spontaneous emission and E_r is the recoil energy). This equilibrium gives a minimal temperature[2] at a detuning $\delta = -\Gamma/2$ given by

$$T_D = \frac{\hbar\Gamma}{4k_B}. \tag{2.10}$$

This is called the Doppler cooling limit. The corresponding atomic velocity for atoms is given by

$$v_D = \sqrt{\frac{\hbar\Gamma}{2m}} \tag{2.11}$$

and is called the Doppler velocity. There are different laser cooling techniques available to overcome this limit, but they are not relevant in this thesis and therefore we will not go deeper into this.

[2] According to the equipartition theorem the kinetic energy of motion is related to the temperature by $\frac{1}{2}mv^2 = \frac{1}{2}k_BT$.

2.3 Magneto-Optical Trapping

In order to keep the cold atoms from diffusing out of the laser beams we need a restoring force. This force should push all the atoms to the same volume in space. This can be achieved by applying a magnetic field gradient, usually a quadrupole magnetic field, over the atoms. This magnetic field gradient causes the energy levels to split. This is also known as Zeeman splitting. The principle of magneto-optical trapping is illustrated in Figure 2.4.

Let's consider an atom with a simple two level system, where the ground state is

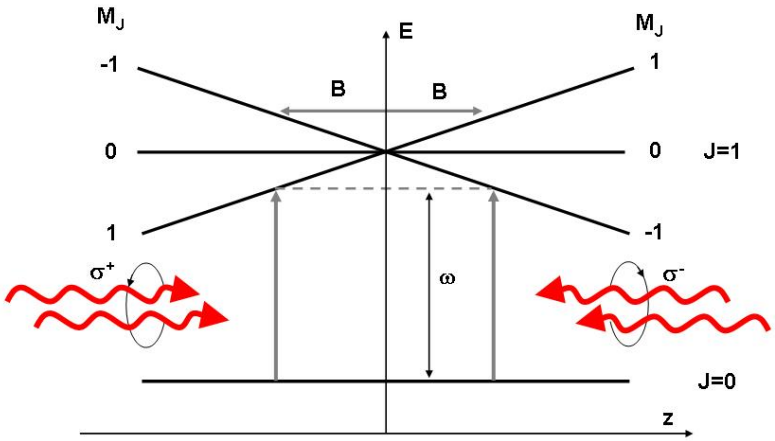

Figure 2.4: *The basic principle of a Magneto-Optical trap for a simple two level atom with J=0 → J=1 transition. Due to the presence of a magnetic field gradient, Zeeman splitting occurs and the magnetic effects on the atom becomes position dependent, which is represented by the oblique lines $M_J = \pm 1$. An atom located on the right side becomes resonant only with the right σ^- laser beam and the atom located on the left with the left σ^+ laser beam.*

characterized with $J = 0$ and the excited state with $J = 1$. If an atom in the ground state $J = 0$ is excited inside a magnetic field gradient to the $J = 1$ state, due to the Zeeman splitting the atom can either be in the sub level $M_J = 0$ or ± 1 depending on the transition rules [11]. This means that an atom will only absorb a photon corresponding to the appropriate magnetic subtransition. If we apply two counter propagating laser beams with the appropriate σ^+ and σ^- polarization and a laser detuning $\delta < 0$ as shown in the illustration, we are able to create a position dependent force that will restore the atoms to the zero B-field region in the center of the trap. We now have a new criterion for when an atom becomes resonant with a laser beam, namely $\delta = \omega_L - \omega_0 + \beta z$ for the $\Delta M = +1$ transition and $\delta = \omega_L - \omega_0 - \beta z$ for the $\Delta M = -1$ transition. The

parameter β, giving the Zeeman shift at displacement z, is given by

$$\beta = \frac{g\mu_B}{\hbar}\frac{dB}{dz} \tag{2.12}$$

where g is the *Landé*-factor and μ_B is the Bohr magneton.
The total force on the atoms in a magneto-optical trap becomes

$$F_{\mathrm{MOT}} = -\hbar k\frac{\Gamma}{2}[\frac{-s_0}{1+s_0+[\frac{2(\delta+kv+\beta z)}{\Gamma}]^2} + \frac{s_0}{1+s_0+[\frac{2(\delta-kv-\beta z)}{\Gamma}]^2}]. \tag{2.13}$$

As in the previous section we can define a capture range z_{cap}, which is the radius where the restoring force is maximal. The optical molasses force given by Equation 2.13, can be simplified for small $v < v_{cap}$ and $z < z_{cap}$ to

$$F_{MOT} \approx -\hbar k s_0 \frac{-2\delta/\Gamma}{[1+s_0+(2\delta/\Gamma)^2]^2}(kv+\beta z). \tag{2.14}$$

As we can see, this force has become velocity and position dependent and can be compared with a damped harmonic oscillator ($F_{\mathrm{MOT}} = -\alpha\dot{z} - \kappa z$), where α is the damping- and $\kappa = \alpha\beta/k$ the spring constant. The force in Equation 2.14 leads to damped harmonic motion of the atoms, where the damping rate is given by $\Gamma_{\mathrm{MOT}} = \alpha/m$ and the oscillation frequency $\omega_{\mathrm{MOT}} = \sqrt{\kappa/m}$. For magnetic fields gradient around 10 G/cm, the oscillation frequency is much smaller (typically few kHz) than the damping rate (typically few hundreds kHz). Thus the motion is overdamped, with a characteristic restoring time τ_R to the center of the trap at $\tau_R = 2\Gamma_{\mathrm{MOT}}/\omega^2_{\mathrm{MOT}}$, which is about a few ms for typical detuning and intensity of the lasers. According to the simplified linear force F_{MOT} from Equation 2.14 the trajectories of the atoms for an overdamped system can be described with

$$z(t) = z_0 e^{-t/\tau}, \tag{2.15}$$

where z_0 is the initial position and $\tau = \frac{\mu_B \nabla B}{\hbar k}$. Here ∇B is the magnetic field gradient $\partial B/\partial x$.

Since the MOT constants α and κ are proportional, the size of the atomic cloud in 3D or the size of the atomic beam in 2D can easily be determined from the temperature. The equipartition of the energy of the system over the degrees of freedom requires that the velocity spread v_{rms} and position spread z_{rms} are related by

$$k_B T = m v^2_{\mathrm{rms}} = \kappa z^2_{\mathrm{rms}}. \tag{2.16}$$

For a temperature in the range of the Doppler temperature the size of the cloud is usually in the order of a few tenths of a mm. Visa versa, from the size of the MOT we could also estimate the temperature.

2.4 Vapor-cell MOT

One way to obtain a cloud of atoms in a MOT is by loading the trap from the background vapor. This is called a vapor-cell MOT. To do so, inside a vacuum with background vapor, six perpendicular laser beams with a diameter around 10-20 mm with

the appropriate polarization are needed, together with a quadrupole magnetic field producing a magnetic field gradient. This is usually obtained by two pair of coils in anti-Helmholtz configuration. In the intersection region of the lasers, only the atoms with a velocity below the capture velocity v_c can be trapped. This capture velocity v_c is different from v_{cap} as we introduced earlier. For a 3D vapor-cell MOT the capture velocity v_c is given by [11]

$$v_c = \sqrt{\frac{d\pi\hbar\Gamma}{\lambda m}}, \tag{2.17}$$

where d is the diameter of the laser beams and λ the wavelength of the trapping laser. Note that for a 3D vapor-cell MOT $v_c > v_{cap}$. Physically this is the maximal velocity for atoms in a laser interaction region to be slowed down and captured in the trap. The principles of this proces are shown in Figure 2.5. Inside the trap two processes occur : the loading of atoms and the loss due to collisions. Slow atoms from the background are loaded into the trap, while at the same time the faster background atoms collide with the cold ones and both leave the trap. Also higher order effects can occur like collisions between two cold atoms. Those will be neglected in this treatment. The number of atoms N in the vapor-cell MOT can be described as

$$\frac{dN}{dt} = R_L - N\Gamma_{BG}, \tag{2.18}$$

where Γ_{BG} is the linear loss rate due to collisions with the background gas and R_L is the loading rate given by

$$R_L = \frac{n_{BG}V^{2/3}v_c^4}{2v_{mp}^3}, \tag{2.19}$$

where n_{BG} is the density of atoms in the background vapor, V the capture volume and v_{mp} the most probable velocity of the background atoms. Solving the differential equation 2.18 for the number of trapped atoms is given by

$$N(t) = \frac{R_L}{\Gamma_{BG}}[1 - \exp(-\Gamma_{BG}t)]. \tag{2.20}$$

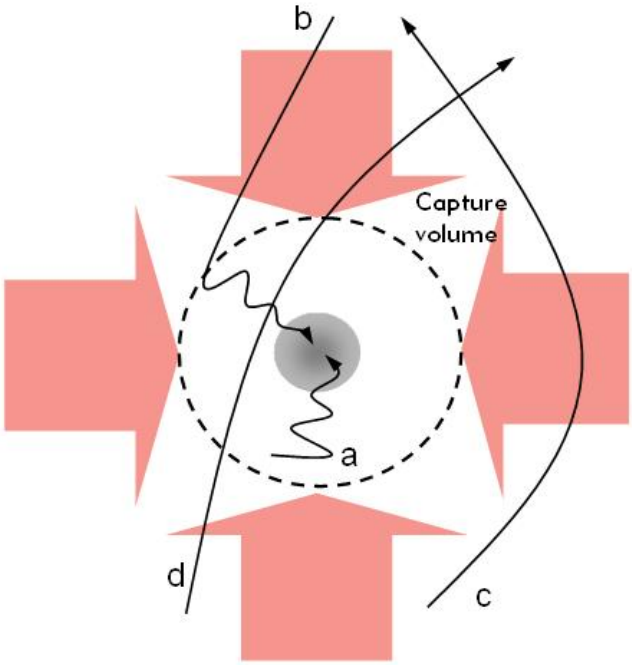

Figure 2.5: *Schematic overview of the working principle of a vapor-cell magneto-optical trap (MOT). Here atoms from the background vapor are trapped into the MOT. The intersection of the laser beams defines the capture volume. Atoms having a velocity below the capture velocity v_c will be captured (a and b). Other will enter the trap but will immediately be rejected.*

2.5 Atomic properties of rubidium

Because of their advantageous atomic properties, alkali atoms are used in many experiments on trapping and cooling of neutral atoms. In our experiments rubidium is used. Rubidium can be found as two different isotopes, ^{85}Rb and ^{87}Rb with a probability of respectively 72.7% and 27.3%. We will use the transition of the ^{85}Rb atoms. The optical transitions from the ground state of rubidium are shown in Figure 2.6. Laser cooling and trapping is done from the ground state $5S(J = 1/2)$ to the fine-structure state $5P(J = 3/2)$. This is done with a trapping laser operated at the closed hyperfine transition $5S_{1/2}(F = 3) \rightarrow 5P_{3/2}(F = 4)$ at a wavelength of 780 nm. Light from this laser also excites off-resonantly the $5P_{3/2}(F = 3)$ state, from which the atoms can decay back to the $5S_{1/2}(F = 2)$ hyperfine level of the ground state. Once the atoms are in this state, they can no longer be excited by the trapping light. Because of this, a repumping laser is applied that pumps the atoms that fall back to the $5S_{1/2}(F = 2)$ state to the $5P_{3/2}(F = 3)$ state, from where they can fall back to the $5S_{1/2}(F = 3)$ state. Table 2.1 gives a list of the relevant laser cooling parameters for ^{85}Rb.

Table 2.1: *Some important characteristic quantities for ^{85}Rb and the laser cycling transitions $5S_{1/2}(F = 3) \longleftrightarrow 5P_{3/2}(F = 4)$. [11]*

Quantity	Symbol	Value
Atomic mass	m	85 a.m.u.=1.41×10^{-25} kg
Wavelength	λ	780.24 nm (in vacuum)
Natural linewidth	Γ	5.98 MHz
Lifetime of $5P_{3/2}(F = 4)$	$\tau = 1/(2\pi\Gamma)$	26.63 ns
Saturation intensity	I_0	1.64 mWcm^{-2}
Recoil velocity	$v_{rec} = \hbar k/m$	0.602 cm s^{-1}
Doppler limit, velocity	$v_D = (\hbar\Gamma/2m)^{1/2}$	11.85 cm s^{-1}
Doppler limit, temperature	$T_D = \hbar\Gamma/2k_B$	142.41μK

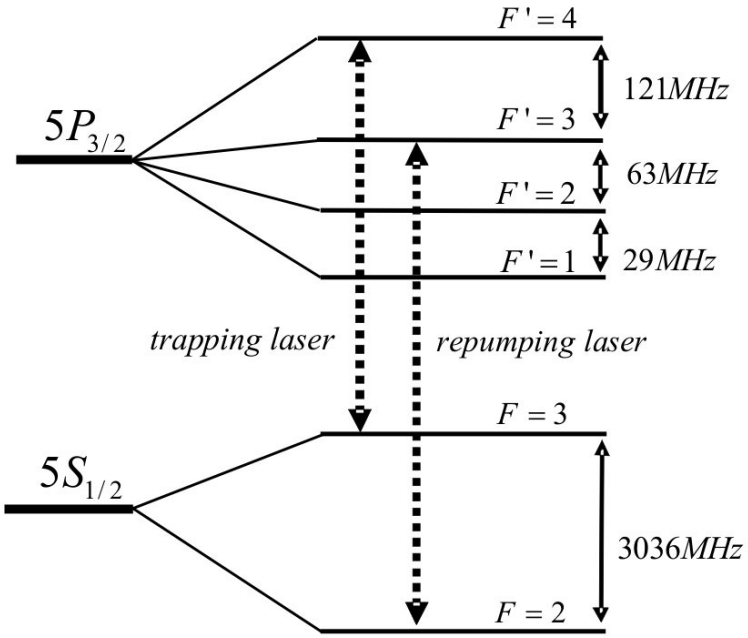

Figure 2.6: *Level diagram and hyperfine structure of* ^{85}Rb *indicating the trapping and repumping laser transition.*

Chapter 3

Two-dimensional magneto-optical trap as source of cold atoms

3.1 The goal of this project

The main goal of the UCP setup is to produce very bright electron and ion bunches. This is described in detail in Claessens *et al.*[6]. In order to make those bright electron or ion bunches, we want a maximum of particles at a maximum density captured in the 3D-MOT that acts as the source. As a consequence, a low background pressure and a high loading rate are required. The loading rate is important since it determines the repetition rate of the electron/ion bunch source. In order to meet these requirements, a two-dimensional magneto-optical trap can be used as a cold atomic beam source to load the 3D-MOT. The advantage of using such an atomic beam source, is that a lower vacuum pressure and higher loading rate can be obtained compared to a vapor cell 3D-MOT. This will increase the lifetime and density of the trapped atoms in the 3D-MOT.

A 2D-MOT produces a cold atomic beam from a vapor cell. In a geometry as shown in Figure 3.1 two pairs of counter propagation laser beams are shone into the vapor cell. These laser beams will cause an optical molasses force and decelerate the atoms velocities v_x and v_y. The velocity of the atoms in longitudinal direction v_z is not changed. In the x- and y-direction a magnetic field gradient creates a restoring force that will push the atoms to the z-axis. This produces two antiparallel, well collimated cold atomic beams along the z-axis. In order to reach the exit of the vapor cell, i.e. through the small differential pumping hole at one side of the cell, the interaction time of the atoms with the laser light needs to be long enough to both slow down the radial velocity of the atom and to force it to the zero B-field axis.
If we add two more laser beams along the atomic beam direction, called a push and retarding beam, we will create a so-called a $2D^+$-MOT. The atomic beam created in the 2D-MOT enters the 3D-MOT. In the 3D-MOT, six orthogonal cylindrical cooling beams and a magnetic field configuration create a trap of cold atoms that will serve as source for the ions or electrons.

In the next section we will start with a summary of existing 2D-MOT systems and

later on we will present some of our results regarding the use of a 2D-MOT in our UCP setup.

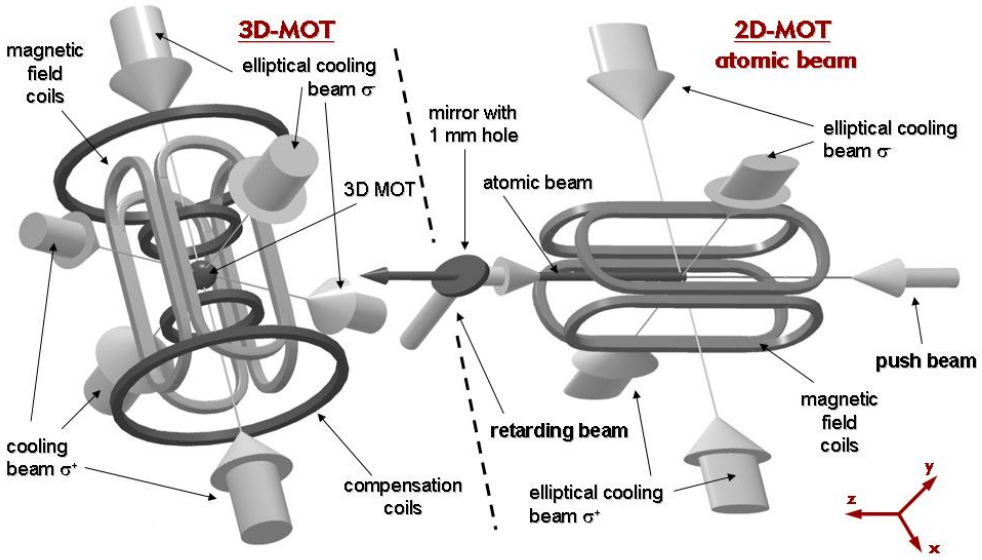

Figure 3.1: *Impression of a 3D-MOT loaded by a atomic beam created by a 2D-MOT as proposed by Dieckmann* et al *[13]. The 3D-MOT is composed out of 6 orthogonal cylindrical cooling beams and a magnetic field configuration for the creation of a quadrupole field. The atomic beam is created by 4 elliptical cooling beams and a magnetic field configuration creating a cylindrical quadrupole field inside a vapor-cell.*

3.2 Summary of recent two-dimensional magneto-optical traps

In this section we will present a summary of recently published work on two-dimensional magneto-optical traps. The design of our 2D-MOT setup is based upon [13] and [14]. Our main purpose to use a 2D-MOT is to increase the loading rate in the three-dimensional magneto-optical trap in order to achieve the desired ion and electron bunches specifications claimed in Claessens *et al.* [6]. This summary will serve as a guide to the experimental results described in the following sections. We will present two different works in order of publication date.

The first review is the work of **Dieckmann *et al.*** published in Phys. Rev. A in 1998 [13]. They present an experimental study of a 2D-MOT for the generation of slow beams of cold atoms from a vapor cell. The experimental setup is similar to our setup as will be described later on. They reported an atomic flux of 9×10^9 rubidium atoms/s at a mean forward velocity of 8 m/s with a width of the velocity distribution of 3.3 m/s full width half maximum (FWHM) and a beam divergence of 43 mrad (FWHM). The experimental study consists of three type of systems: a 2D-MOT, a $2D^+$-MOT and a

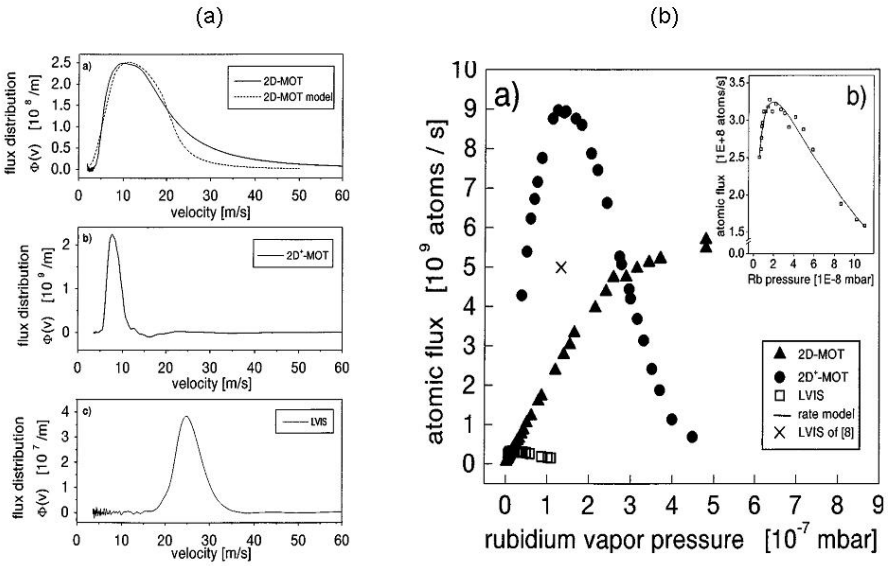

Figure 3.2: *(a) Foreword velocity distribution of the flux from a 2D-MOT, 2D$^+$-MOT and LVIS. (b) Flux of the atom beam versus rubidium vapor pressure for three different configurations. [13]*

so-called LVIS [16] configuration. We are only interested in the first two configurations, especially the difference between them. Important to realize is that the experiments where done with small cooling beams characterized by a beam waist radius of w_z=24 mm and $w_{x,y}$=7 mm. Here w is defined such that the intensity distribution is proportional to e^{-2r^2/w^2} with r the beam radius. Also a low laser power, maximum around 34 mW, is used. From their results we can conclude that upgrading the 2D-MOT to a 2D$^+$-MOT results in an increase of total flux of rubidium atoms and a more narrow forward velocity distribution with lower mean velocity, as we can see in Figure 3.2(a). In Figure 3.2(b) the atomic flux of the beam is presented as function of rubidium vapor pressure for all three configurations. We see that there is a significant difference in both velocity distribution and total flux between the 2D-MOT and 2D$^+$-MOT. Furthermore, we can observe that the 2D$^+$-MOT creates a higher atomic flux at lower Rb vapor pressure and reaches a maximum around 1×10^{-7} mbar. For the 2D-MOT we see that the flux increases linearly up to 5×10^{-7} mbar without reaching a maximum.

The second review of a two-dimensional magneto-optical trap is the work of **Schoser *et al.*** published in Phys. Rev. A in 2002 [14]. They present a 2D-MOT setup for the production of a continuous collimated beam of cold ^{87}Rb atoms from a vapor cell. Also their experimental setup is similar in concept with our setup. They measured a total flux of cold Rb atoms of 6×10^{10} atoms/s and a small divergence of 32 mrad. The longitudinal velocity distribution of the atomic beam showed a broad feature (FWHM around 75 m/s) centered around 50 m/s. The dependence of the flux on laser intensity, on geometry of the trapping volume, and on rubidium vapor pressure where investigated in detail. Most important difference with the previous work of Dieckmann *et al.*

is that they used a 2D-MOT with larger cooling beams (laser waist radius w_z up to 45 mm) and higher laser power (up to 160 mW per laser beam). Furthermore, they give a simple model for the velocity distribution of the flux based on rate equations describing the general features of their source. Some of the results obtained are presented in Figure 3.3. In the article the measurement of the atomic flux as function of velocity is compared with results from their model. From these results we can conclude that the presented model gives an accurate description of the dynamics of the 2D-MOT. Later, they added a push beam, with a diameter of 5 mm, to the 2D-MOT setup and presented the flux as function of velocity distribution for several push beam intensities. Here only experimental results are presented. This pushing beam is aligned perpendicular to the cooling beams and shines along the axis copropagating with the atoms and has the same detuning as the cooling beams. The result is shown in Figure 3.4 where a narrow (width ≈7.5 m/s) and intense peak at low velocities (centered around 25 m/s) arises.
In Table 3.1 an overview of both rubidium 2D magneto-optical traps is given.

Table 3.1: *Overview of the most important 2D-MOT parameters presented by Dieckmann* et al. *[13] and Schoser* et al. *[14].*

	max. flux	$\langle v_z \rangle$	FWHM	divergence	$w_z, w_{x,y}$	laser power
Dieckmann *$2D^+$-MOT*	9×10^9 atoms/s	8 m/s	3.3 m/s	43 mrad	24 , 7 mm	34 mW (max)
Schoser *2D-MOT*	6×10^{10} atoms/s	50 m/s	75 m/s	32 mrad	45 ,15 mm	640 mW (max)

3.3 A model for the 2D-MOT

In this section we will present a model for the flux of cold atoms generated by a 2D-MOT source. This model is based on the rate equation model introduced by C. Monroe [15] for a vapor cell MOT and later expanded for an atomic beam source by Dieckmann *et al.* [13] and Schoser *et al.* [14]. This model describe the atomic flux as function of the various parameters as the size of the laser beams and the atomic density in the vapor cell n. In the next section we will expand a 2D-MOT by introducing a push beam and model the atomic flux in this configuration.

The atomic flux generated by the 2D-MOT source is built out of two parts. The first part is $\Psi(n, v_z, z)$, the influx of atoms from the vapor cell that is cooled and compressed to an atomic beam. Here n is the vapor density, v_z the velocity component of the vapor along the atomic beam axis and z the position with respect to the exit hole. Secondly there is a survival probability for the atoms to reach the exit hole $\exp(-\Gamma_{\text{coll}}(n)z/v_z)$ due to light assisted collisions between the cold atomic beam and the background vapor. We than define a function $\tilde{\Phi}(n, v_z)$ which describes the flux per velocity interval

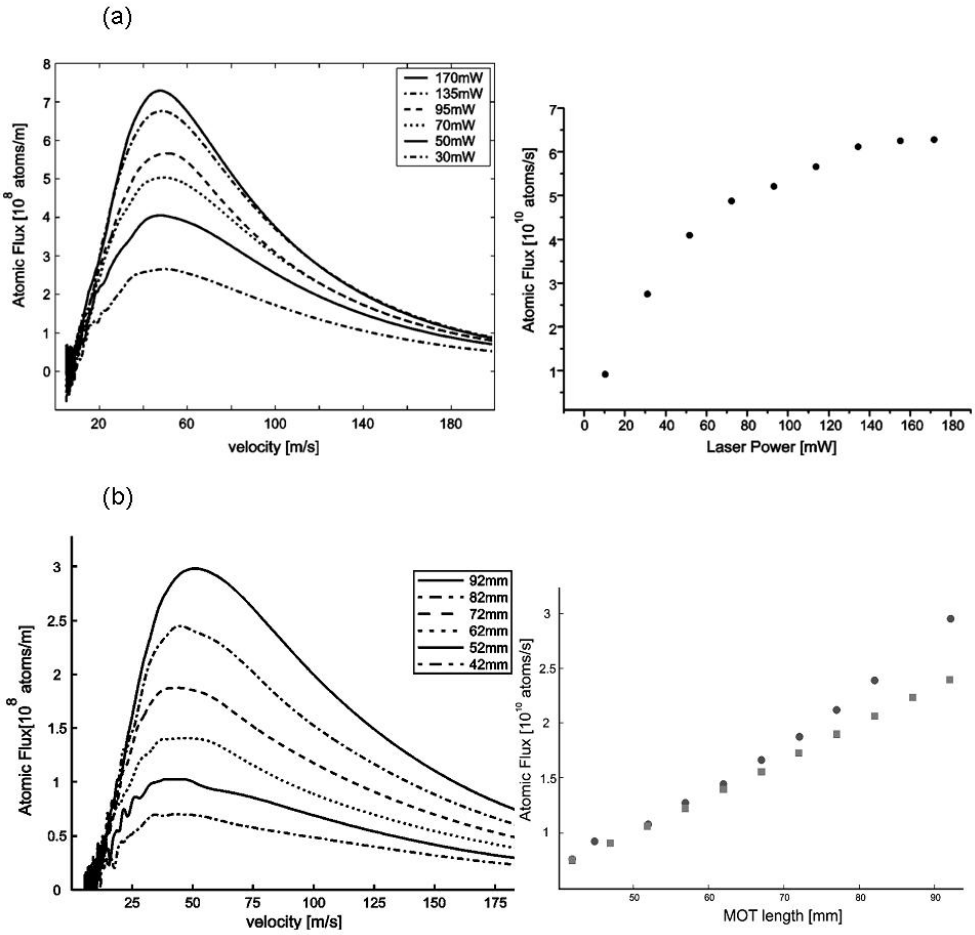

Figure 3.3: *(a, left) Distribution of atomic flux versus longitudinal velocity for different laser power in the cooling beams. The velocity distribution is centered around 50 m/s and has a width of about 75 m/s. (a, right) Total atomic flux versus total laser cooling power per beam. (b,left) Distribution of atomic flux versus longitudinal velocity for different length of the MOT beams. The power per laser beam was kept constant at 21 mW. (b,right) Total atomic flux versus length of the cooling volume. [14]*

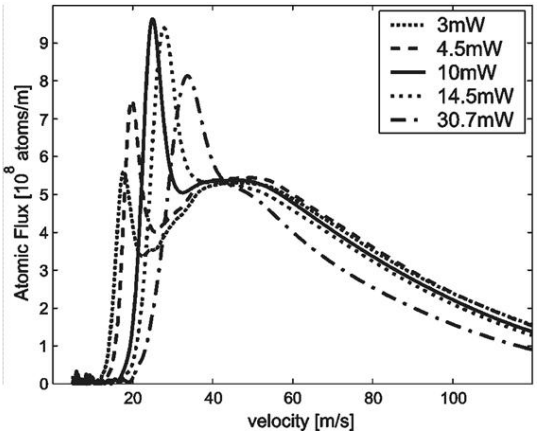

Figure 3.4: *Distribution of atomic flux versus longitudinal velocity when a laser beam is shone on the axis copropagating with the atomic beam. We see that the velocity distribution changes dramatically. A narrow (width ≈7.5 m/s) and intense peak at low velocities (centered around 25 m/s) arises. [14]*

$[v_z, v_z + dv_z]$ as

$$\tilde{\Phi}(n, v_z) = \int_0^L \Psi(n, v_z, z)\exp(-\Gamma_{\text{coll}}(n)z/v_z)dz, \tag{3.1}$$

where $\Gamma_{\text{coll}} = n\langle v\rangle\sigma_{\text{coll}}$, $z/v_z$is the time of flight for the atoms through the MOT volume and L the size of the laser beams (2× the beam waist w_z). According to Dieckmann *et al.* [13], the effective collision cross section for losses out of the beam is found to be $\sigma_{\text{coll}} \approx 3\times10^{-12}$ cm^{-2}. Here they assume that Rb atoms only interact with the vapor background through a C_3/R^3 potential (resonant dipole-dipole interactions). To calculate the total flux coming through the differential pumping tube, we need to integrate $\tilde{\Phi}(n, v_z)$ over all longitudinal velocities

$$\Phi_{tot} = \int_0^\infty \tilde{\Phi}(n, v_z)dv_z. \tag{3.2}$$

Note that for the flux in one direction, only the positive longitudinal velocities v_z are taken into account.

The next step in the model is to generate the function $\Psi(n, v_z, z)$ that describes the influx of atoms from the vapor cell that is cooled and compressed and will contribute to the atomic beam flux. Therefore we consider a cooling volume with a diameter d, defined as 2× the beam waist $w_{x,y}$, and a length L. The influx within this volume is proportional to the atomic density in the vapor cell and only radial velocities smaller than the capture velocity generate the beam. All velocities need to be weighed according to Maxwell-Boltzmann statistics. The influx contributing to the atom beam becomes [14]

$$\Psi(n, v_z, z) = nd\frac{16\sqrt{\pi}}{u^3}\exp(-v_z^2/v_{mp}^2) \times \int_0^{v_c} v_r^2\exp(-v_r^2/v_{mp}^2)dv_r, \tag{3.3}$$

where $v_{mp} = \sqrt{2k_BT/m}$ is the most probable velocity of the Maxwell-Boltzmann distribution, $v_r = \sqrt{v_x^2 + v_y^2}$ the radial velocity and v_c the capture velocity. This capture

velocity v_c is a function of v_z and z. According to Schoser *et al.* [14] the capture velocity can be modeled as

$$v_c(v_z, z) = \frac{v_{c0}}{1 + 2dv_z/Lv_{c0}} \tag{3.4}$$

where v_{c0} is the capture velocity for particles with $v_z = 0$. Note that for small v_z the capture velocity $v_c \approx v_{c0}$ and for large v_z the capture velocity $v_c \propto 1/v_z$.

This model can be used to generate the flux of a 2D-MOT as function of the longitudinal velocity distribution for several parameters such as the dimensions of the cooling volume, the capture velocity and the density.

As we will see in Chapter 5, we will measure the loading rate of the 3D-MOT Π_{3D} using the 2D-MOT as source of rubidium atoms. Here the loading rate Π_{3D} is similar to R_L in Equation 2.18 but now for a 3D-MOT loaded from an atomic beam instead of a background vapor. Using the rate equation model introduced above we can define the loading rate as

$$\Pi_{3D} = \xi \int_0^{v_c^{3D}} \tilde{\Phi}(n, v_z) dv_z \tag{3.5}$$

where v_c^{3D} the capture velocity of the 3D-MOT and ξ is the divergence capture fraction and is given by

$$\xi = \begin{cases} (\frac{v_D}{\langle v_z \rangle \theta_{\max}})^2 & \text{if } \frac{v_D}{\langle v_z \rangle} > \theta_{\max} \\ 1 & \text{otherwise} \end{cases} \tag{3.6}$$

where v_D is the Doppler velocity, $\langle v_z \rangle$ the average velocity of the flux and $\theta_{\max}$ the maximum allowed divergence. Due to geometric limitations, the allowed divergence of the beam is limited. The parameter ξ gives the fraction of atoms from the beam reaching the 3D-MOT given a maximal allowed divergence angle θ_{max} and beam divergence $\theta_{beam} = v_D/\langle v_z \rangle$.
This model will be used to understand and explain our results. In the next section we will expand this model by adding an extra push beam.

3.3.1 Push beam model

If we combine Equation 3.1 and 3.3 we obtain the flux distribution as function of longitudinal velocity. Now we can evaluate Equation 3.1 for v_z from $[-\infty, \infty]$ instead of $[0, \infty]$ to obtain a symmetric distribution that represents both atomic beams generated by the 2D-MOT. One beam is traveling in positive z-direction and the other beam in negative z-direction. Now we add a push beam to the system. A push beam is a laser beam along the z-axis with same detuning as the four cooling beams. This beam causes an optical molasses force in the z-direction and (1) will slow down and reverse some fraction of the beam traveling in negative z-direction and (2) increase the forward velocity of the beam in positive z-direction. The aim is to increase the total flux toward the 3D-MOT and change the velocity distribution. To model this final flux distribution using a push beam, we calculate the velocity change Δv_z for the distribution $\tilde{\Phi}(n, v_z, z)$

caused by a cooling force $F_{push}(v_z)$ in positive z-direction given by

$$F_{\text{push}}(v_z) = -\hbar k \frac{\Gamma}{2} \frac{s_0}{1 + s_0 + (2(\delta - kv_z)/\Gamma)^2}. \tag{3.7}$$

The velocity change Δv_z is given by

$$\Delta v_z = \frac{1}{m} \int_0^t F_{\text{push}}(v_z) dt. \tag{3.8}$$

Here t is the time that the atoms interact with the push beam. If we assume that the flux is created in the center of the 2D-MOT, around $z = L/2$, the velocity change Δv_z of the atomic flux towards the 3D-MOT will be calculated by integrating Equation 3.8 until the atoms reach the pumping hole at $z = L$. The flux with a component in the negative z-direction has to be decelerated to v_z=0 before the atoms reaches $z = 0$. The atoms that can be reversed will be re-accelerated back towards the 3D-MOT and will add up to the final flux distribution.

Chapter 4

Experimental setup

4.1 Two-dimensional magneto-optical trap

The basic geometry of the experimental setup (see Figure 4.1) is given by a vapor cell separated from the main vacuum chamber by a differential pumping hole with a diameter of 1 mm. This pumping hole is also used as output for the atomic beam and maintains a pressure drop around an order of magnitude between vapor cell and main vacuum chamber. The vapor cell consists out of a standard glass cuvette (30×30×150 mm^3) glued to a metal construction with epoxy. Between the vapor cell and the main vacuum chamber a cross is mounted where on one side a tube is placed that is connected to an ion-getter pump. On the other side of the cross a small tube leads to a pipe filled with rubidium. This pipe can be heated up to 90 ^oC to increase the rubidium vapor pressure in the vapor cell. A set of four racetrack-shaped coils is placed around the vapor cell to generate the cylindrical quadrupole field with a line of zero magnetic field along the symmetry z-axis. A main current source (0-15 A), which flows through all four coils in serie, produces a variable magnetic field gradient up to 22 G/cm. Four separate small current sources (0-2.5 A) are placed in parallel with each racetrack-shaped coil to be able to move the zero magnetic field axis in x- and y-direction by creating an unbalance in the current true each coil.
The laser system used for the two-dimensional magneto-optical trap is described in the next section. For the trapping beams, a power up to 100 mW is available. Note that the total usable laser power, approximately 200 mW, has to be divided between the 2D- and 3D MOT system. For the 2D-MOT we used four separate ($\sigma^+ - \sigma^-$ polarization) cylindrical cooling beams. Two beam pairs, counter propagating, are perpendicular to each other and to the atomic beam axis, defined as the zero field z-axis produced by the MOT coils. The four cooling beams have an elliptical cross section with a larger waist radius w_z=52 mm along the atomic beam axis and a smaller waist radius $w_{x,y}$=13 mm perpendicular to it.
Later on in the experiments the 2D-MOT is extended to a $2D^+$-MOT, by adding two additional laser beams parallel to the atomic beam axis.

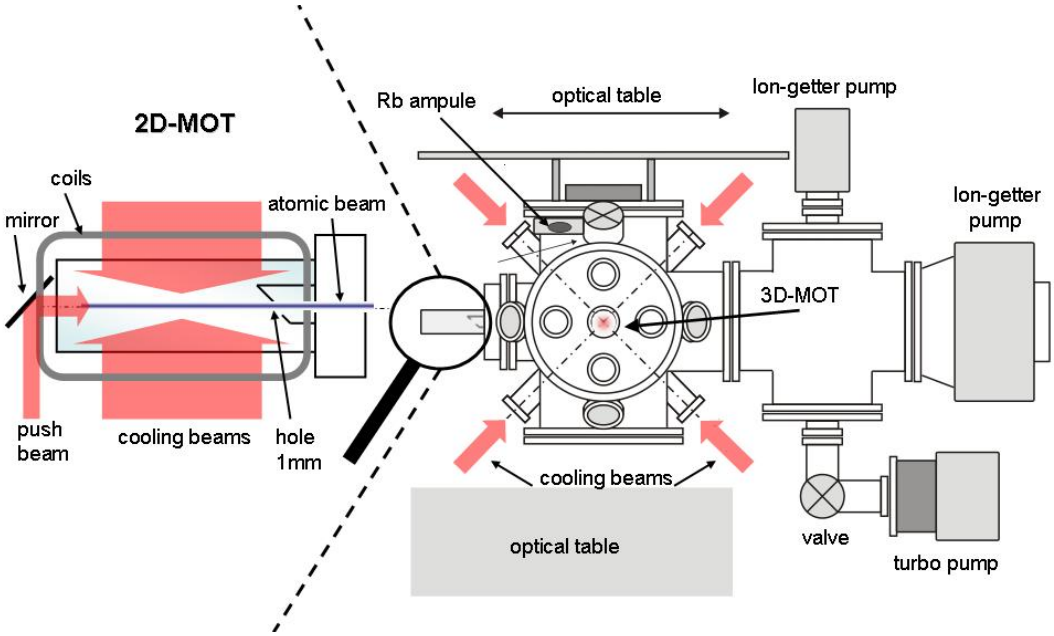

Figure 4.1: *Illustration of the vacuum setup. A central trap chamber can be pumped down by three separate vacuum pumps. Two ion getter pumps and one turbo molecular pump that can be isolated from the trap chamber by a manual valve. Above the setup an optical platform is placed for the optics to steer the MOT beams. To load the MOT with rubidium atoms a vapor-cell is located on the left, connected by a 1 mm hole with the main chamber. Here an atomic beam is created by a 2D-MOT. A MOT can also be loaded directly from a Rb ampule that is connected to the main chamber.*

4.2 Three-dimensional magneto-optical trap

The basic geometry of the three-dimensional magneto-optical trap setup is given in Figure 4.1. The 3D-MOT will serve as our main diagnostic tool for the characterization of the atomic beam source (2D-MOT). To obtain a 3D-MOT a vacuum system is needed. To increase the number of trapped atoms the pressure inside the vacuum system has to be sufficient low, in the order of 10^{-9} mbar, to reduce the elastic and inelastic collisions with the hot background particles. These condition are obtained using an ion-getter pump. One way for the atoms to reach the system, is by heating a rubidium ampul which is connected to the vacuum chamber with a mechanical valve. By adjusting that valve and controlling the temperature of the rubidium holder, the rubidium vapor pressure in the main vacuum chamber can be regulated. Another way to bring the rubidium into the 3D-MOT system, is by using the 2D-MOT as an atomic beam source. In this case, no additional rubidium vapor is needed in the main vacuum chamber which leads to a lower pressure due to reduced collisions between the atoms in the trap and the background vapor. Due to some geometry limitations, the atomic beam leaving the differential pumping hole in the 2D-MOT is limited to a divergence of $\leq$60 mrad. For a divergence >60 mrad a fraction of the total atomic beam will not reach the center of the 3D-MOT. As described in Chapter 2, also a magnetic field gradient is needed to trap atoms. This gradient is generated by a pair of coils in anti-Helmholtz configuration. The magnetic field gradient can reach 20 G/cm at maximum current (around 200 A). For the 3D-MOT typical laser saturation intensities s_0 are between 1-10 for all six laser beams combined and the diameter is typically 1 cm.

4.3 The laser system

An important part of this setup are the lasers. To build 2D and 3D-MOT from rubidium atoms, two stable and powerful lasers are needed. The frequency stability of the trapping laser should be better than the natural atomic line width of approximately 6 MHz.
The trapping laser, in this case is a commercial diode laser (Toptica DLX) generates approximately 950 mW at a wavelength of 780 nm. This power has te be split up to generate both the 3D- and 2D-MOT. Usually the power distribution is about 50/50.
The second one is the repump-laser, also a commercial diode laser (Toptica DL 100) generates 150 mW at a wavelength of 780 nm. This laser serves as repump laser for both the 2D- and 3D-MOT with again a power distribution around 50/50. The setup of both lasers is shown in Figure 4.2. The laser setup is mounted on an optical table with shock absorbing rubbers to reduce vibrations.
To lock the trapping- and repump-laser on the proper transition, a spectroscopy method is used [12]. In the feedback system the light is sent through an acousto-optical modulator (AOM). In a AOM the photons of the original laser beam interact with the phonons in the crystal that are generated by a computer controlled rf signal. The laser beam coming out of the AOM is now shifted in frequency. So by adjusting the AOM, the frequency of the laser beam can adjusted. This is done for both 2D-MOT and 3D-MOT laser beams separately. To increase the efficiency of the AOM we use a telescope to collimate the beam. The stability of the laser was measured to be better than 1 MHz

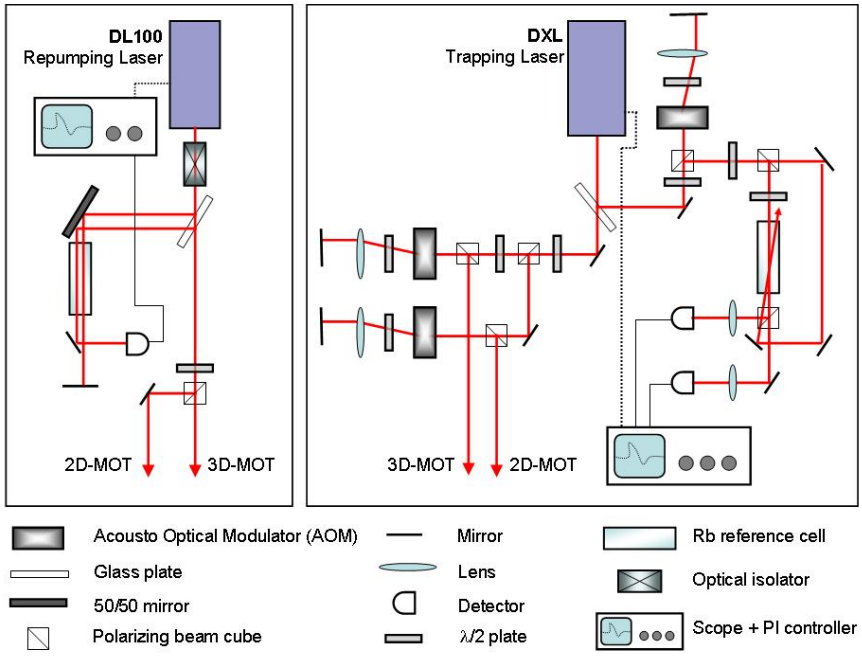

Figure 4.2: *Schematic overview of both trapping and repump laser is given. Also a detailed overview of the locking system is given.*

[9], smaller than the 5.98 MHz natural line width. Both lasers beams can be detuned separately.

4.4 Diagnostics

4.4.1 Number of trapped atoms and loading rate

In order to characterize the cloud of cold Rb atoms in the 3D-MOT, it is imaged with two calibrated CCD cameras and the fluorescence is detected with a photo diode. This system is shown in Figure 4.3. The fluorescence power P of a MOT is given by

$$P = \hbar\omega\Gamma f N, \tag{4.1}$$

where N is the number of trapped atoms, $\hbar\omega$ the energy of the emitted photon, Γ the decay rate from the excited state and f the fraction of atom in the excited state. This is given by

$$f = \frac{1}{2}\frac{s}{1+s+4\delta^2/\Gamma^2}, \tag{4.2}$$

where s is the total saturation parameter of all 6 laser beams together. In the calculations we will assume ***f=1/2***, which gives us an underestimate of the total number of atoms N. These diagnostics are described more in detail by Kusters [18]. The photodiode signal provides the data for loading and lifetime measurements by monitoring the scope signal $N(t)$. The size and number of atoms in the trap are obtained by fitting

the CCD images with a 2D-Gaussian function [18]. From this fit the size, position and number of trapped particles can be estimated. The calibration of the CCD cameras was done using a low intensity laser beam shone on the CCD and measured with a calibrated (Newport 840) Optical Power Meter. The spot was fitted for a range of laser intensities and different exposure time for the CCD. The number of trapped particles fluctuates with 5-10%.

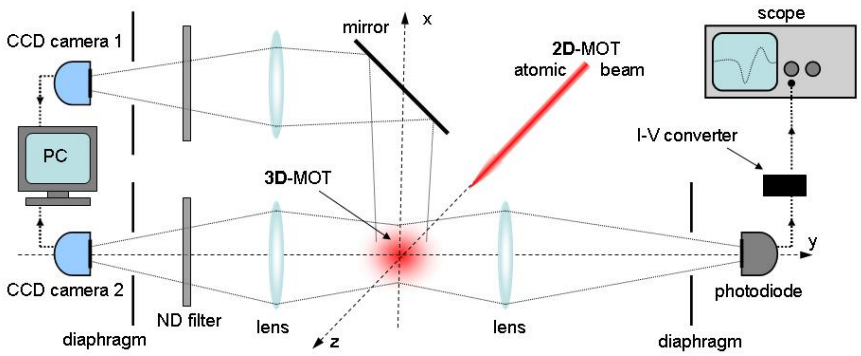

Figure 4.3: *Schematic overview of the CCD camera and photodiode setup. Two calibrated CCD cameras are posisioned to image all dimensions (x,y,z) of the MOT. The images are analyzed by a computer. The photodiode is connected to a I-V converter and monitored by a scope.*

4.4.2 Rubidium vapor pressure measurement

Using absorption spectroscopy in the vacuum system for the 2D vapor-cell MOT it is possible to estimate the Rb-vapor pressure. According to Dieckmann *et al.* [13] the Rb-vapor pressure at room temperature, i.e. at T=20^{o}C, is p_{ref} 2.4×10^{-7} mbar. The absorption spectroscopy setup used to estimate the Rb-vapor pressure is shown in Figure 4.4. To calibrate the system a reference Rb test cell with length x_{ref}=80 mm, at room temperature T_{ref}=20^{o}C, is placed into a low intensity laser beam ($s_0 \ll 0.1$). The absorption ratio between the vapor-cell and reference cell is given by

$$\frac{\Delta I_{\mathrm{vc}}}{\Delta I_{\mathrm{ref}}} = \exp(-\frac{p_{\mathrm{vc}} x_{\mathrm{vc}}}{p_{\mathrm{ref}} x_{\mathrm{ref}}}), \tag{4.3}$$

where p_{vc} is the Rb-vapor pressure and x_{vc} = 42 mm the length that the laser beam travels in the vapor-cell. The temperature in our vapor-cell is also T_{vc}=20^{o}C. The absorbtion spectra from the test-cell and from the vapor-cell are shown in Figure 4.5. From Equation 4.3 the vapor pressure in the cell p_{vc} is calculated. By heating the Rb-source the vapor pressure can be increased. From the absorption spectra measured at different source temperature the vapor pressure in the vapor-cell was found to be ranging between 0.5×10^{-8} and 5×10^{-8} mbar for source temperatures between 20^{o}C and 80^{o}C. These pressures are significantly lower than the values of Dieckmann *et al.* [13]. Our setup was operated with a continuous ion-getter pump running. Without the ion-getter pump the pressure inside the vapor-cell increased to values where it was not possible to create a 2D-MOT anymore. We studied the pressure increase and

observed that this increase was not caused by rubidium vapor. The increase in Rb vapor pressure was only a minor effect. Although we are not sure about the cause of the pressure increase, a leak in the 2D-MOT setup might be at the origin of the problem and has to be investigated more in detail next time the vacuum in the setup will be broken.

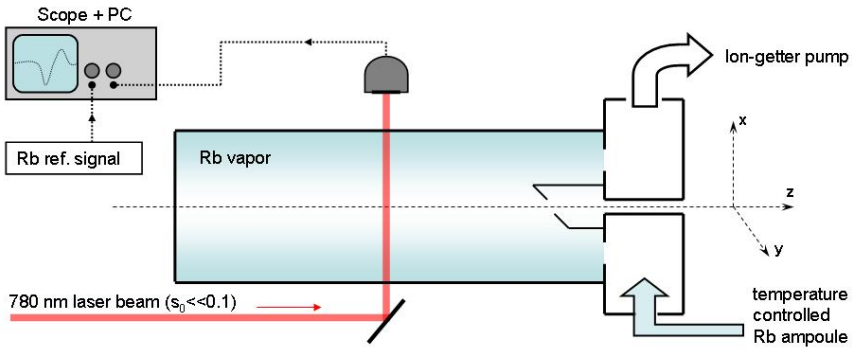

Figure 4.4: *Schematic overview for the measurement of the Rb vapor pressure in the 2D-MOT glass cell using absorption spectroscopy. A low intensity laser beam passes through the vapor-cell and is detected with a photodiode. This laser is scanned across resonance and photodiode signal is compared with a reference signal from a calibrated Rb test vapor-cell at room temperature. An example of both absorption signals is shown in Figure 4.5.*

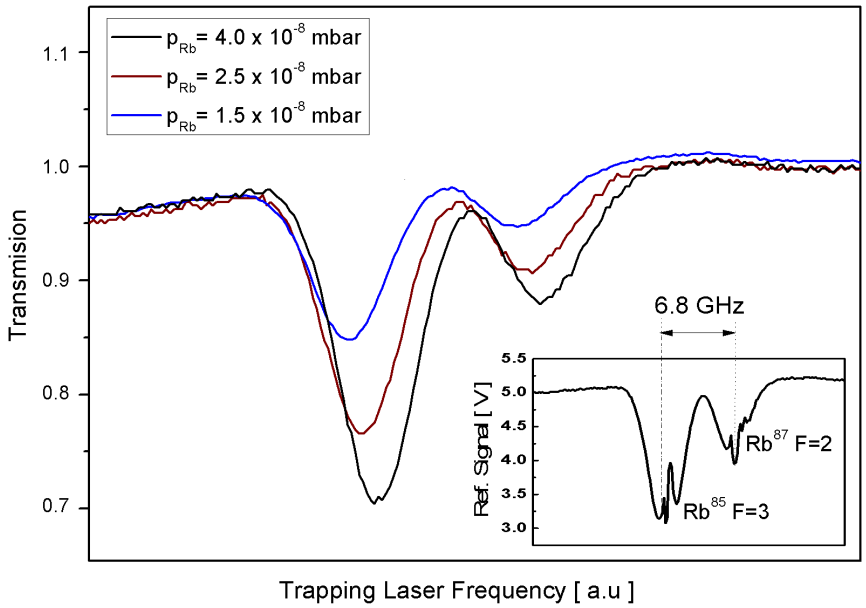

Figure 4.5: *The absorption spectra for three different rubidium vapor pressures. In the lower right corner the reference spectra for rubidium is shown. The left peak is the* $^{85}Rb\ 5^2S_{1/2}$ *F=3 line and the right peak is the* $^{87}Rb\ 5^2S_{1/2}$ *F=2 line.*

Chapter 5

Experimental Results

5.1 Loading of the 3D-MOT from vacuum background

In this section we determine an important property of the three-dimensional magneto-optical trap, namely the loading rate R_L from a background vapor. Measuring and optimizing the loading rate is an important measure for the performance of our entire setup. Later in this chapter this loading rate will be the most direct measure to characterize out 2D-MOT. Now we will first introduce the origin of it and the way to measure this loading rate. Later on in this thesis another loading rate will be introduced, namely the loading rate of the 3D-MOT from an atomic beam, defined as Π_{3D}. The aim of this experimental research project is to increase the loading rate and the lifetime of the 3D-MOT.

As we already described in Chapter 2, atoms from the background vacuum are captured and can be loaded into the magneto-optical trap. The rate at which the slow atoms enter this volume can be approximated by

$$R_L \approx \frac{nd^2v_c^4}{v_{mp}^3} \tag{5.1}$$

where n is the background Rb density, d is the laser beam diameter and $v_{mp} = (2k_BT/m)^{1/2}$ is the most probable velocity of the atoms in the background vapor at a given temperature T. In our experiments we measure the number of trapped atoms as function of time. This describes the loading of the MOT from the background vapor. These measurements are shown in Figure 5.1 for various laser detuning δ. These measurements where done by switching on and off the magnetic field gradient so that the atoms in the trap could be ejected to $N = 0$. From the loading of the trap we can measure the influence of the loss mechanism, that is the collisions with background vapor $\Gamma_{BG} \approx n\sigma u$, where σ is the cross section from background gas collisions that eject a trapped atom. In Chapter 2, Equation 2.18 described the loading a magneto-optical trap. The solution for this differential equation is given in Equation 2.20 and is used to fit the loading measurements as shown in Figure 5.1.

Typical loading rates R_L ranges between $1{\times}10^7$ and $5{\times}10^7$ atoms/s. The corresponding lifetimes ($\tau = 1/\Gamma_{BG}$) where found to be 2 s to 3 s. The steady-state solution

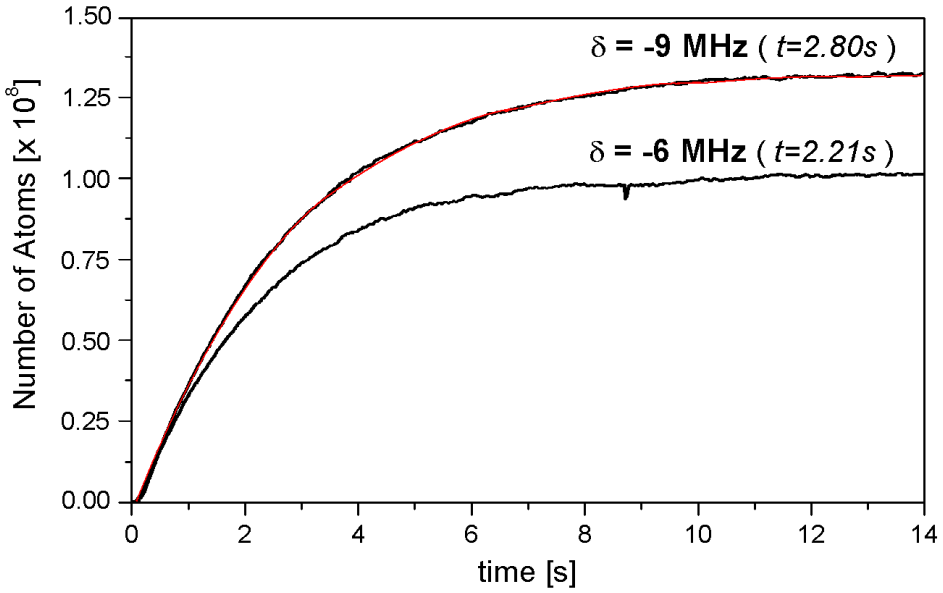

Figure 5.1: *The number of atoms in the 3D-MOT loaded from background Rb vapor for two different laser detuning δ after switching on the magnetic field in the trap. The red line shows the fit using Equation 2.20 to determine the loading rate R_L and lifetime τ.*

$\partial N/\partial t = 0$ gives us the total number of trapped atoms

$$N_{ss} = \frac{R_L}{\Gamma_{BG}}. \tag{5.2}$$

The total number of atoms trapped was found to be in the order of 1.3×10^8 atoms.

By rewriting Equation 5.1 we are able to estimate the room temperature Rb partial pressure p_{Rb} in the vacuum system from R_L by

$$p_{Rb} \approx \frac{R_L k_B T}{\pi^2 d^2 v_c^4} [\frac{2\pi k_B T}{m}]^{3/2}. \tag{5.3}$$

We find p_{Rb} =8×10^{-10} mbar, using a diameter of the laser beams of d=15 mm, a temperature T = 300 K, a capture velocity for the 3D-MOT v_{c0}= 35 m/s using Equation 2.17 and the measured loading rate R_L=5×10^7 atoms/s. From the ion-getter pump current the Rb background pressure was estimated to be in the order of 1×10^{-9} mbar. We can conclude that these values matches very well.

Now we have found a value for the loading rate and the lifetime of our setup. If we want to optimize our setup we will have to increase those two values: $R_L \geq 5 \times 10^7$ atoms/s and $\tau \geq 2$ s.

5.2 2D-magneto-optical trap experiments

As we described in Chapter 3 we will investigate the potential increase of the loading rate and the lifetime in the 3D-MOT by using a cold atomic beam source (2D-MOT) to load the atoms in the 3D-MOT. The only diagnostic tool available to characterize our atomic beam source is the loading Π_{3D} and lifetime τ of the 3D-MOT. In the next subsections a study of the 2D-MOT performance is presented as function of various experimental parameters. The results are compared with the model described in section 3.3 and with the results presented in [13] and [14].

5.2.1 Cooling volume dependence

The cooling volume of the 2D-MOT is defined by the length L and the diameter d of the cooling beams. Since we hare elliptical laser beams, we will define the larger axis as the length L (z-axis) and the smaller axis as the diameter d (x- and y-axis). Based on the theoretical model, the flux of cold atoms from a 2D-MOT source given by Equation 3.1, suggests that increasing the length of the 2D-MOT leads to a higher flux. The higher flux comes from the longer cooling time $\tau = L/\langle v_z \rangle$, so faster atoms can be captured when increasing the length L. For large values of L this increase trend to saturate when the cooling time τ becomes larger than the collision time $1/\Gamma_{coll}$. The length L is this measurement is defined as the total length of the laser beams shone into the vapor cell.

Figure 5.2 shows the loading rate of the 3D-MOT versus the length L of the laser beams in the 2D-MOT. This measurement was done by successively blocking a part of all four cylindrical MOT beams, starting on the back side of the glass cuvette. During this measurement the intensity of each beam was kept constant. The total intensity per beam was 1.1 mW/cm^2 ($s_0 \approx 2.7$) and the cylindrical beam had a Gaussian shape in both x- and y-direction with a waist radius of respectively $w_z = 50$ mm and $w_{x,y} = 13$ mm. Note that the length of the MOT is defined as the total length of the cylindrical laser beam from the aperture up to the blocking cone, i.e. the length (2× waist radius) of the laser beams. This means that the intensity I is not constant over the entire cooling surface. From Figure 5.2 we see that the loading rate increases with length up to a certain value where it saturates. The increase of loading rate is in general agreement with the predictions of our model in Equation 3.1. The saturation might be due to the intensity decrease of the laser beams. At 75 mm the intensity of the laser beam has dropped to about 40 % of I_{tot}.

The same investigation is done for the beam diameter d. By using a "home made" aperture the radial diameter of the cooling beam was varied (without changing the length L) while the loading rate was measured. The results are shown in Figure 5.3 where the loading rate and laser beam intensity are shown as function of vertical beam radius ($d = 2r$). From Equation 3.1 we see that the flux increases proportionally with the beam diameter d. This agrees with the flux increase predicted by our model (See Equation 3.3). The loading rate trends to saturates at a beam radius of 15 mm for the same reasons as proposed in the previous study.

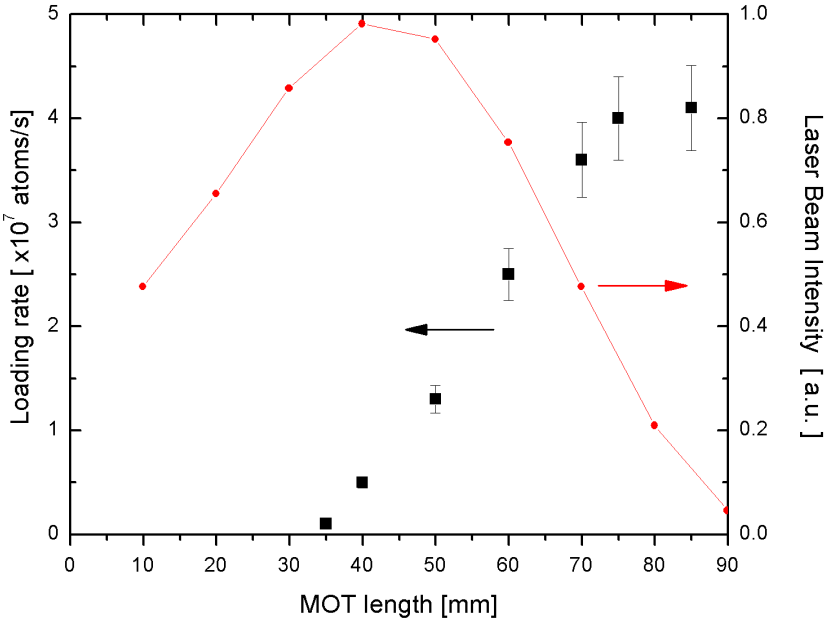

Figure 5.2: *Loading rate of the 3D-MOT as function of the length of the 2D-MOT. The intensity profile of the horizontal laser beam is shown in red.*

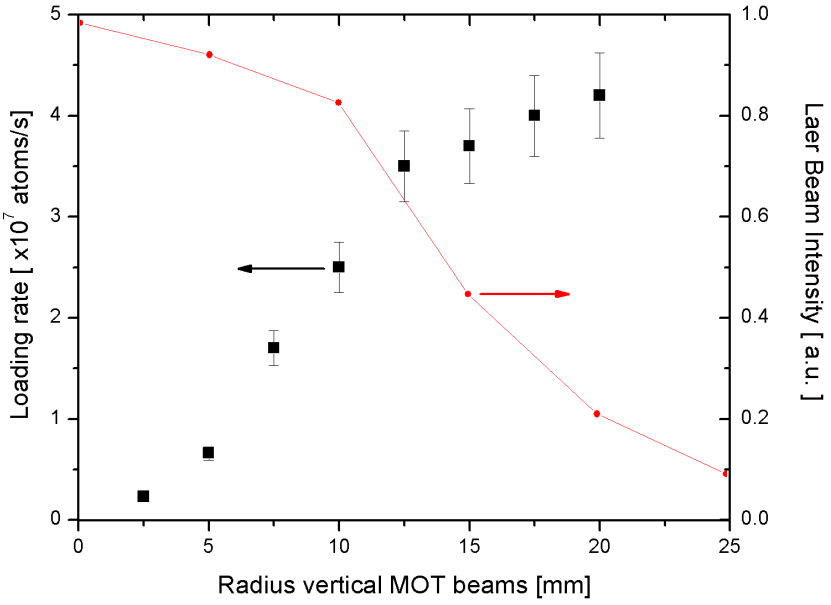

Figure 5.3: *Loading rate of the 3D-MOT as function of the radius of the vertical 2D-MOT beams. The intensity profile of the vertical laser beam is shown in red.*

5.2.2 Rubidium vapor pressure dependence

A variation of the rubidium vapor pressure is done by changing the temperature of the Rb ampule holder. In the current setup we were only able to vary the pressure over a narrow pressure range as we presented in Section 4.4. The measured Rb vapor pressure was ranging between 1×10^{-8} and 5×10^{-8} mbar. The Rb vapor pressure was measured by absorption spectroscopy as explained in Section 4.4. Figure 5.4 shows the dependence of loading rate Π_{3D} on the vapor pressure in the 2D-MOT vapor cell. We see that the loading rate increases linearly with vapor pressure. This is in agreement with our model (Equation 3.1). For low densities n the flux of the atomic beam increases proportional to vapor density ($\tilde{\Phi}(n, v_z) \propto n$). The saturation limit is not reached because the maximum pressure is still very low. Using our model we simulate the velocity distribution of the flux for a rubidium vapor pressure of $4.5{\times}10^{-8}$ mbar. The relation between pressure and density was calculated by $n = p/k_B T$, where p is the vapor pressure and T the temperature of the vapor. The velocity distribution for our atomic beam source was calculated using our model and is shown in Figure 5.5. We observe that at this very low density the forward velocity v_z of the atoms is centered around 2 m/s with a FWHM of 4 m/s. This is a very low forward velocity. To compare with the normal operating vapor pressure used by Dieckmann *et al.* [13]($p = 2 \times 10^{-7}$ mbar), we showed the velocity distribution at this pressure in the right upper corner of Figure 5.5. We see that mean forward velocity increases to 12 m/s with a FWHM of 20 m/s.

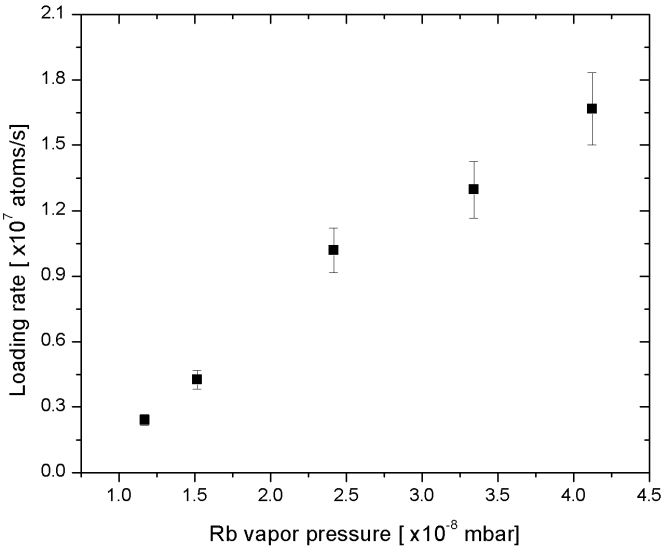

Figure 5.4: *Loading rate of the 3D-MOT as function of the Rb vapor pressure in the glass cell. The Rb vapor pressure was measured using absorption spectroscopy.*

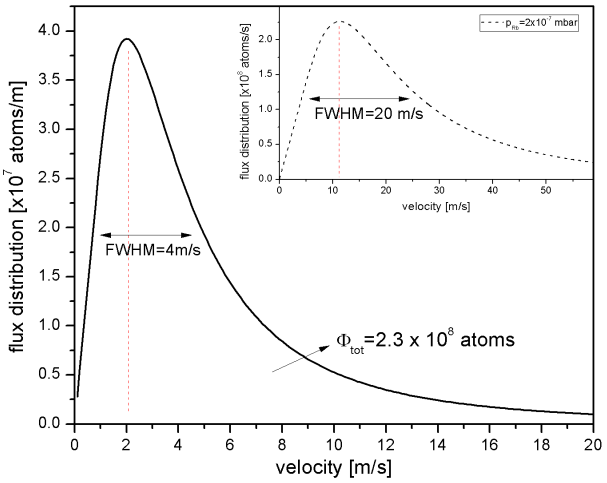

Figure 5.5: *Flux distribution for a 2D-MOT with a Rb vapor pressure of 4.5×10^{-8} mbar. In the right upper corner the flux distribution of plotted for a Rb vapor pressure of 2×10^{-7} mbar.*

Consequences of very low vapor pressure

Unfortunately, we where not able to obtain a Rb vapor pressure above 5×10^{-8} mbar. Due to this very low vapor pressure, not only a low atomic flux can be obtained, but from our rate equation model we found that the longitudinal velocity of the atoms is very low. This flux is centered around $\langle v_z \rangle = 2$ m/s with a FWHM of 4 m/s. The emerging atomic beam leaving the differential pumping hole will therefore have a large divergence. We can estimate this beam divergence by $\theta \approx \langle v_r \rangle / \langle v_z \rangle$. We consider $\langle v_r \rangle \geq v_D = 0.12$ m/s, where v_D is the Doppler velocity. This results in a RMS beam divergence $\geq$60 mrad. As we already presented in Chapter 3, the maximum allowed divergence of the atomic beam, based on our geometry, is $\theta_{\max} \approx 50$ mrad. That means that an important fraction of the atomic beam will not reach the 3D-MOT. In the model for the loading rate Π_{3D} this is taken into account with the parameter ξ (See Equation 3.6). As we can see from Equation 3.6 ξ can be improved by increasing the average longitudinal velocity of the atomic beam. The average velocity of the beam needs to be large enough to lower the beam divergence, well below 50 mrad, but has to stay below the capture velocity of the 3D-MOT which is around $v_c = 30$ m/s. Later we will see that this can be achieved using a push beam.

5.2.3 Laser intensity dependence

By varying the total laser power of the cooling beams for the 2D-MOT, the loading rate of the 3D-MOT was measured as function of laser intensity. The laser intensity was measured with a calibrated (Newport 840) Optical Power Meter with a sensor area of 1 cm^2. The four cooling beams have an elliptical cross section with (in this case) a larger waist radius w_z=40 mm along the atomic beam axis and a smaller waist radius $w_{x,y}$=12 mm perpendicular to it. The results are shown in Figure 5.6 where the dependence of the loading rate on the total laser intensity is plotted.

Increasing the laser intensity I leads to a higher capture velocity v_c. This is also experimentally observed by Schoser *et al.* [14] and can be understood by studying the nature of the capture velocity. The capture velocity v_c is defined as the maximal velocity an atom can have to be captured in the intersection of the laser beams with a diameter d, given the time t it interacts with the laser beams. Atoms with $v > v_c$ will escape from the MOT and atoms with $v \leq v_c$ will be captured. Mathematically,

$$\frac{1}{m}\int_0^t F_{\mathrm{MOT}}(v,x)dt = v_{c0}, \tag{5.4}$$

with the initial and final condition that $x(0) = 0$, $x(t) = d$ and $v(t) = 0$. Here d is the laser beam diameter. To study the dependence of the laser intensity I on the capture velocity v_c we solve Equation 5.4 numerically as function of $s_0 = I/I_0$. The results of the simulation are shown in the Appendix.

Next we simplify Equation 3.1 and Equation 3.5 to obtain a simple and visible dependence of the loading rate Π_{3D} on capture velocity. By considering that at very low vapor pressures the average forward velocity $v_z < v_c^{3D}$ and $v_c \ll u$ we can simplify Equation 3.1 to

$$\Pi_{3D} \approx \xi n d v_{c0}^3 \frac{16\sqrt{\pi}}{u^3 \Gamma_{\mathrm{coll}}} \int_0^{v_c^{3D}} v_z[1 - \exp(-\Gamma_{\mathrm{coll}}\frac{L}{v_z})]dv_z. \tag{5.5}$$

Because v_c and $v_z \ll u$ we assumed $\exp(-v_r^2/u^2) = \exp(-v_z^2/u^2) \approx 1$ and for small v_z the capture velocity $v_c \approx v_{c0}$.

Now it is possible to compare the laser intensity dependence on the loading loading rate, using Equation 5.5, with the experimental results presented in Figure 5.6. From Equation 5.5 we can see that $\Pi_{3D} \propto v_{c0}^3$. For higher intensities ($I > 2$ mW/cm^2), corresponding to a total laser power between 55-90 mW, this corresponds well with the experimental results as we can see from the dotted line in Figure 5.6. For lower intensities, corresponding to a total laser power beween 15-55 mW, the loading rate Π_{3D} increases linearly, from a certain intensity ($I_{tot} \approx 1.5$ mW), as function of the total laser intensity. This can be undrstood by considering that increasing laser intensity cause power broadening of the atomic spectral lines. Also at higher intensities the magneto-optical potential becomes steeper resulting in a higher compression of the atomic beam which increase the probability of passage of the atoms in the atomic beam through the hole. This linear increase is also simulated and measured by Chaudhuri *et al.* [17].

5.2.4 Magnetic field gradient dependence

In Figure 5.7 the loading rate of the 3D-MOT is shown as function of the magnetic field gradient in the 2D-MOT. Increasing the magnetic field gradient leads to a higher spring constant on the atoms inside the capture volume. But increasing the gradient leads also to a decrease in capture range. This capture range can be calculated by

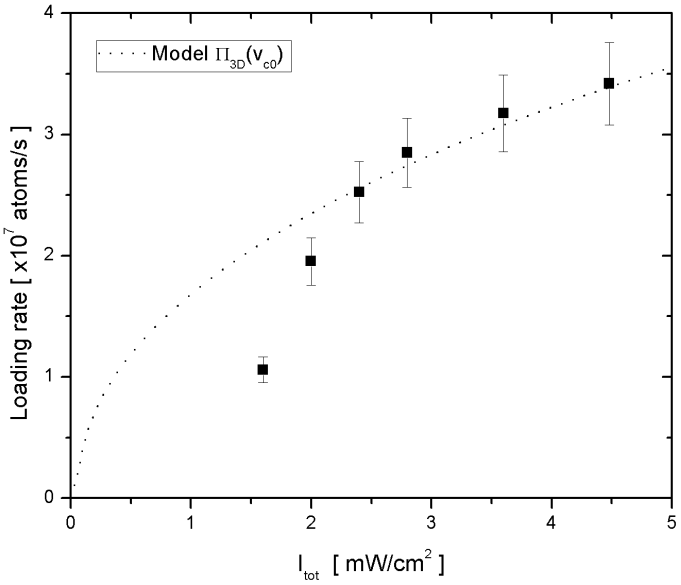

Figure 5.6: *Loading rate of the 3D-MOT as function of the total laser intensity for the four elliptical laser beams combined of the 2D-MOT. The dotted line represents the trend of the loading rate versus gradient using the approximation* $\Pi_{3D} \propto v_{c0}^3(s_0)$.

$x_c = \hbar\gamma/\mu_B \nabla B_r$ and determines together with the length of the laser beams the volume in which atoms experience a compression force. In Figure 5.7 we see a decrease of the loading rate for magnetic field gradients above 14 G/cm, which corresponds to a capture range of 2.86 mm. This capture range will also influence the capture velocity v_c, which is a parameter that can be used to estimate the loading rate Π_{3D} using Equation 5.5. Again we solved Equation 5.4 numerically as function of the magnetic field gradient ∇B. These results are shown in the Appendix. Previously we saw that $\Pi_{3D} \propto v_{c0}^3$, so the numerical results for v_{c0} versus ∇B were calculated and the model $\Pi_{3D} \propto v_{c0}^3$ is plotted as a dotted line in Figure 5.7 to compare with the experimental results. We see that the experimental data and model follows the same trend but reaches a maximum at a different value.

5.2.5 Laser detuning dependence

In Figure 5.8 the loading rate of the 3D-MOT is shown as function of the laser detuning δ of the 2D-MOT. The trend observed in Figure 5.8 agrees well with the measurements done by Chaudhuri *et al.* [17] for the total flux from a 2D$^+$-MOT as function of laser detuning. Again we used our model from Equation 5.5 to study the variation of the capture velocity as function of laser detuning. By solving Equation 5.4 as function of laser detuning $v_{c0}(\delta)$ (see Appendix) and fill the result in Equation 5.5 we find the dotted line in Figure 5.8. This dotted line reaches a maximal value at a different laser detuning as observed in the measurements and seems to have a steep decrease for

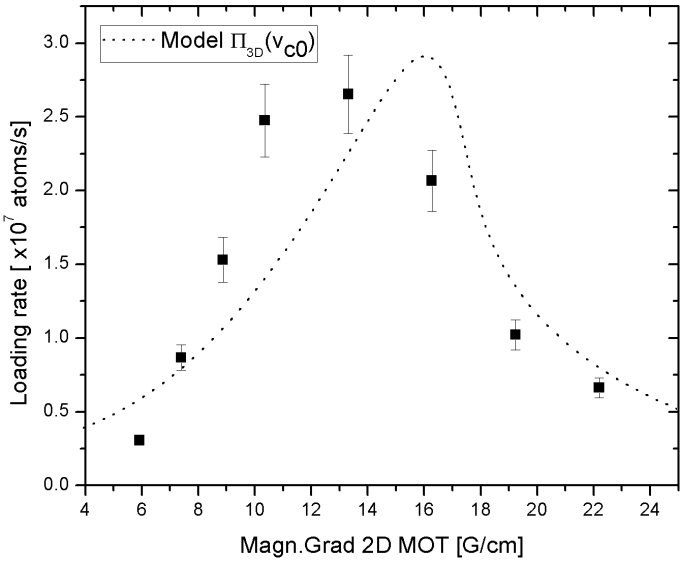

Figure 5.7: *Loading rate of the 3D-MOT as function of the magnetic field gradient of the 2D-MOT. The dotted line represents the trend of the loading rate versus gradient using the approximation* $\Pi_{3D} \propto v_{c0}^3(\nabla B)$.

$\delta/\Gamma < -2.5$. Important to notice is that during the measurement it was only possible to measure the relative change in laser detuning. Therefore we calibrated the laser detuning by choosing $\delta/\Gamma = 0$ where the 2D-MOT disappeared completely. In the measurement done by Chaudhuri *et al.* [17] we see that we can find zero flux at a laser detuning $\delta/\Gamma = -1$. This leaves us with an uncertainty in the calibration of the absolute laser detuning of about $\delta = \Gamma$, which corresponds to 6 MHz. If we shift the data over 6MHz, the model shows in general the same trend as our measured data.

5.2.6 Push beam

In addition to the four counter propagating laser cooling beams we shone in an extra laser beam of the same detuning along the axis of the atomic beam. The intensity of the push beam was set at $s_0 \approx 2$ and the optimal diameter of the push beam was found to be $d = 5$ mm. As we already discusses in the modeling section this beam will have two positive effects on the loading rate of the 3D-MOT Π_{3D}. (1) First the part of the beam that was traveling in the opposite direction of the 3D-MOT can now be slowed down and eventually accelerated in the direction of the 3D-MOT. This will potentially increase the loading rate Π_{3D}. (2) Secondly the atoms in the beam traveling towards 3D-MOT will experience an acceleration and will end up with a higher average forward velocity (in case of low Rb vapor pressures). This will decrease the divergence of the beam leading to a more efficient loading.

In Figure 5.9 the loading curves of the regular 2D-MOT and the 2D-MOT with push beam are presented for different detuning of the laser beams. We observe a significant increase in loading rate Π_{3D}, up to 10× the loading rate achieved with a conventional

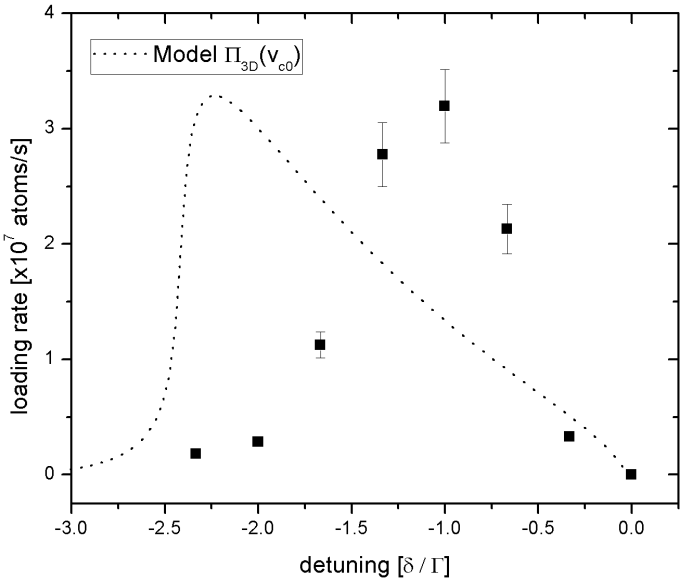

Figure 5.8: *Loading rate of the 3D-MOT as function of the laser detuning of the 2D-MOT. The dotted line represents the trend of the loading rate versus gradient using the approximation* $\Pi_{3D} \propto v_{c0}^3(\delta/\Gamma)$.

2D-MOT as we observed from our measurements. The highest loading rate observed using a push beam was $\Pi_{3D} = 5 \times 10^8$ atoms/s. In Figure 5.9 we see that the loading curve with the highest loading rate, curve (a), does not have the normal shape as expected from Equation 2.20. The loading rate is so high that the MOT keeps growing up to a point where the loading stops due to the limitations in maximum density imposed by rescattering of photons and light-assisted collisions. Later we will see that in this regime unstable behavior of the MOT can occur.

To study the effects of a push beam on the 2D-MOT we built a computer program to simulate the interaction of the flux from the 2D-MOT with a laser beam over a certain distance as we discussed in Section 3.3. The flux distribution $\tilde{\Phi}(v_z)$ generated by Equation 3.1 is supposed to originate in the center of the 2D-MOT and has a component in both directions. The beam running towards the 3D-MOT will be accelerated over a distance $L/2$ and the beam moving towards the push beam will be decelerated. A part of the decelerated beam will be re-accelerated in the direction of the 3D-MOT and will add to the other beam. Atoms that exit the interaction region before they can be reversed, will not take part in the final beam. In this model we assume that all atoms that will switch from direction will be able to be trapped again and pass to the exit hole. To test the model we generated an initial flux distribution with the conditions as used by Schoser *et al.* [14] in the experiments with a push beam (See Figure 3.4). We simulated the final flux distributions $\tilde{\Phi}(v_z)$ for two different intensities of the push beam. The simulation results are shown in Figure 5.10. Both the initial and final flux distributions are presented and can be compared with Figure 3.4.

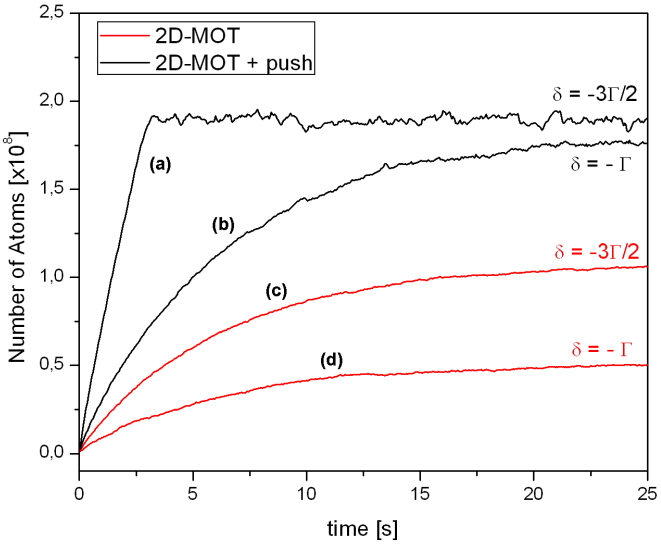

Figure 5.9: *Loading of a 3D-MOT using a 2D-MOT with (a),(b) and without (c),(d) push beam for different laser detuning.*

We see that our model generates nearly the same flux distribution as measured by Schoser. By increasing the intensity of the push beam we see that the peak increases in height and shifts towards higher velocities. This trend was also observed by Schoser. From this result we conclude that our model approximates well the effects of a push beam on the flux distribution and will be used to study our own experiments.

In Figure 5.11 we show a simulation of the velocity distribution from the atomic flux using Equation 3.1 for a regular 2D-MOT and for a 2D-MOT with a push beam. The conditions of this experiment where the same as the one used in Figure 3.4. Using the push beam we can observe that the average forward velocity is shifted from 3 m/s towards a higher velocity around 10 m/s. This will reduce the divergence of the atomic beam by a factor of 3. Due to this reduction in divergence the atomic beam will load the 3D-MOT more efficiently (see Equation 3.6). Secondly, since the initial flux distribution has a very low average velocity (3 m/s), the flux which initially moved in the opposite direction can be decelerated and redirected toward 3D-MOT. Both effects will contribute to the increase in loading rate Π_{3D}, up to 10×, observed experimentally.

5.2.7 2D$^+$ MOT

We started this chapter by giving an overview of two 2D-MOT systems as source of slow atoms. Our setup was based on elements of both systems. The aim was to make a 2D$^+$-MOT, which according to Diekmann *et al.* [13] should boost up the atomic flux by an order of magnitude compared to a conventional 2D-MOT. The 2D$^+$-MOT

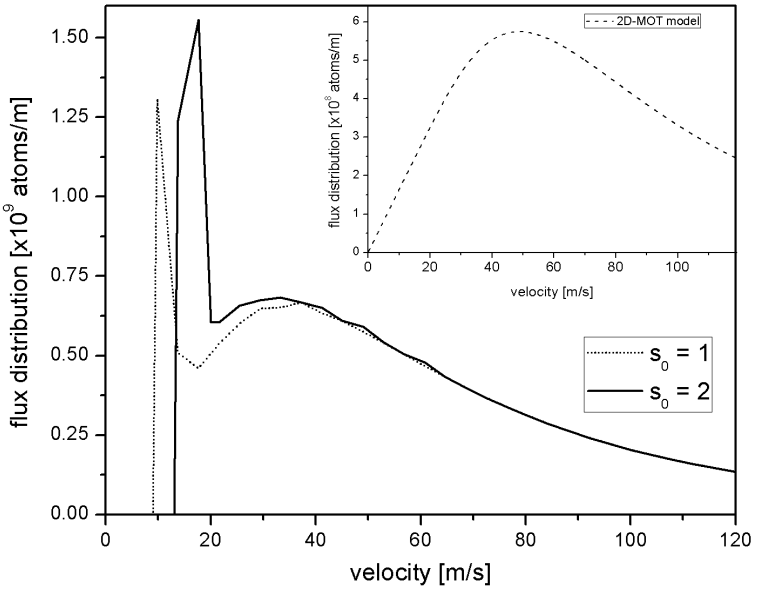

Figure 5.10: *The final flux distribution for the experiment as given in Figure 3.4 using a push beam of $s_0 = 1$ and $s_0 = 2$ using our simulation model. The initial 2D-MOT flux distribution used as input for the simulation is shown in the right upper corner with a dotted line.*

is an extension of the 2D-MOT with a push beam, as in the previous subsection, and a retarding beam as shown in Figure 3.1. This configuration was built and tested on our setup. However, we where not able to observe the expected significant increase in loading rate of the 3D-MOT as soon as we add a retarding beam. Experiments where the ratio between push and retarding beam is varied showed that the highest increase in loading rate Π_{3D} was achieved for a ratio of 100/0 (% of push/retarding-beam).
From this measurement we conclude that only a push beam is necessary to increase the loading rate (total flux). To show this, we used our push beam model to generate the initial flux distribution using Equation 3.1 for the conditions used by Dieckmann in the experiments showed in Figure 3.2. First the initial distribution was compared with the measured flux distribution for Figure 3.2 for a 2D-MOT, which seems to agree very well. Next we simulated the effects of a push beam on this initial flux distribution. The result is shown in Figure 5.12. Both the initial and final flux distribution are presented. Using our push beam model we are able to simulate almost the same final distribution as Dieckmann measured with the $2D^+$-MOT. From this simulation we conclude that the huge increase achieved in Dieckmann *et al.* [13] is essentially due to the push beam.

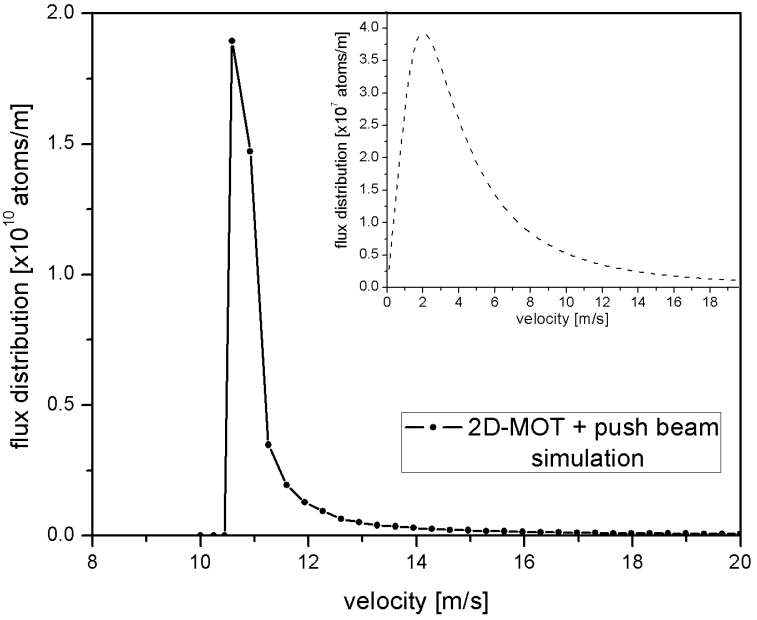

Figure 5.11: *The finial flux distribution using a push beam of 1 mW generated using our simulation model. The initial 2D-MOT flux distribution, for a* $p_{Rb} = 4.5 \times 10^{-8}$ *mbar, used as input for the simulation is shown in the right upper corner with a dotted line.*

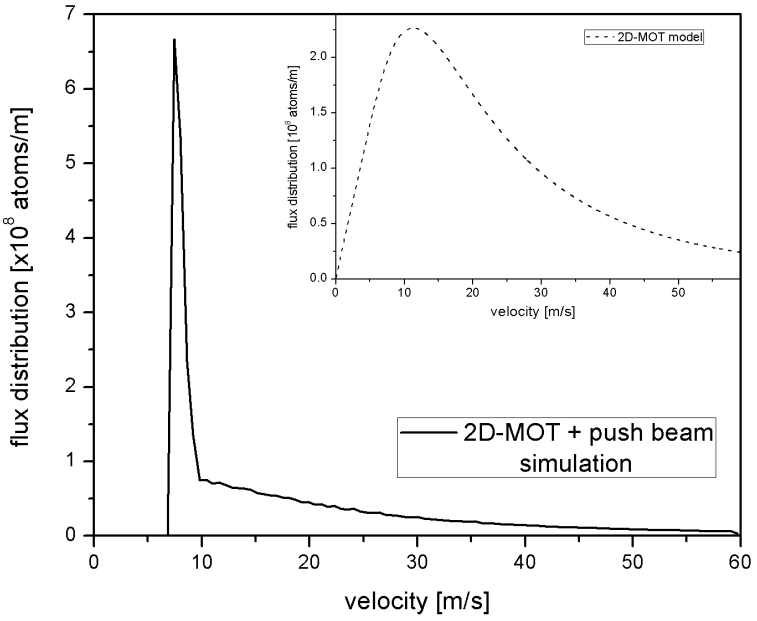

Figure 5.12: *The finial flux distribution using a push beam of 0.5 mW generated using our simulation model. The initial 2D-MOT flux distribution used as input for the simulation is shown in the right upper corner with a dotted line.*

5.2.8 Lifetime of the MOT

By creating a 3D-MOT from the rubidium background vapor, i.e. a vapor-cell MOT, it was not possible to measure the lifetime of the MOT directly. The numbers given in Section 5.1 gives the loading time of the MOT with can be calculating from the loading curve. For a MOT in equilibrium this loading time is equal to the lifetime of the MOT. For a vapor-cell MOT we found a lifetime between 2 and 3 seconds.
By using an atomic beam from a 2D-MOT to load the 3D-MOT is was possible to measure the lifetime of the MOT directly by suddenly switching off the atomic beam. An example of such a measurement is shown in Figure 5.13. From these measurements it was possible to calculate the lifetime directly. For a MOT loaded by an atomic beam using a 2D-MOT we found a lifetime between 8 and 12 seconds, which is a 4× increase.

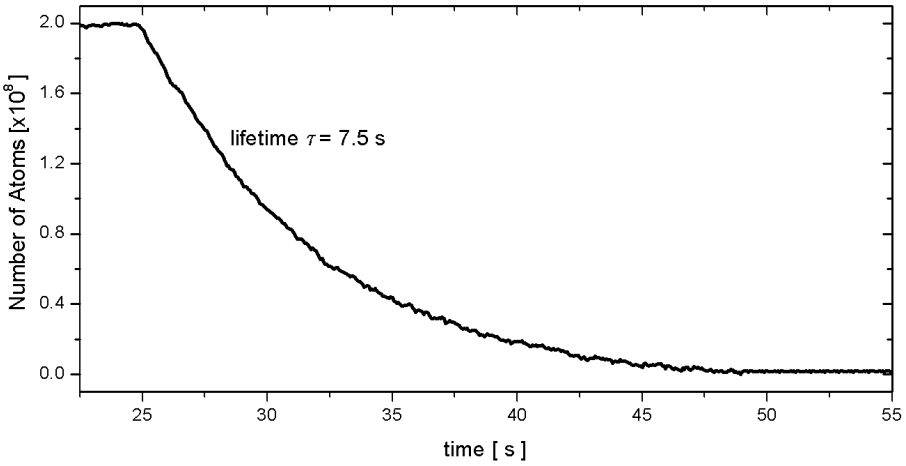

Figure 5.13: *The number of atoms in the MOT as function of time for the loading using a 2D-MOT with push beam. At t=25 s the 2D-MOT is swithed off. The exponential decrease characterize the lifetime of the MOT. The lifetime of this measurement is about 7.5 s.*

5.2.9 Conclusions

The aim of this research was to increase both the loading rate and lifetime of the 3D-MOT. Using a vapor-cell MOT we were able to achieve a loading rate up to 5×10^7 atoms/s and a lifetime up to 3 s.
Although the experiments were done at very low rubidium vapor pressure ($p_{Rb} \approx 5 \times 10^{-8}$ mbar) we found that the loading rate could be increased up to 5×10^8 atoms/s using a 2D-MOT with push beam for the loading of the MOT. Here we found a lifetime up to 10 s. If we could use this technique at higher rubidium vapor pressure, around $p_{Rb} \approx 5 \times 10^{-7}$ mbar, it will be possible to increase the loading rate even by an order of magnitude ($\approx 5 \times 10^9$ atoms/s).

5.3 Instabilities in the magneto-optical trap

In some of the loading measurements we could observe unstable behavior of the magneto-optical trap. The variations in number of trapped atoms observed where clearly different than the noise variations typically found in previous experiments. In Figure 5.14 the number of atoms in the trap is shown at four different laser detuning of the 3D-MOT ($\Delta\delta = 0.4$ MHz). In the bottom graph the population variations are less than 2% and are induced by random fluctuations. In the three other graphs we can observe a significant oscillation, up to 10% in number of atoms all with a different frequency ranging from 0.5 Hz to 2 Hz.
Recent studies have shown that the collective behavior of the atomic cloud produced by a MOT exhibits both stochastic and deterministic instabilities [29]. A model demonstrates that the different stochastic behavior observed in the experiments are well explained if the absorption of light by the atoms is taken into account through the so called shadow effect [30]. The shadow effect is a phenomenon that can occur when a MOT is built with retroreflective optics. When the laser beam passes through the MOT the intensity is partially absorbed but this laser beam also severs as counter propagating beam. Because both counter propagating beams are not equally distributed in term of intensity, the MOT is irregularly cooled. This effect is called the shadow effect. In this work we will not focus on a detailed study of such effects, but we only want to make clear that this kind of instable behavior of the MOT can have important consequences on the stability of the ion or electron bunches. This will cause brightness fluctuation in the same order as the population fluctuations.
According to [29] and [30], a solution to avoid these instabilities is to build a 3D-MOT with 6 separate laser beams instead of retroreflective optics as used in our setup. This could prevent the shadow effect that causes these instabilities.

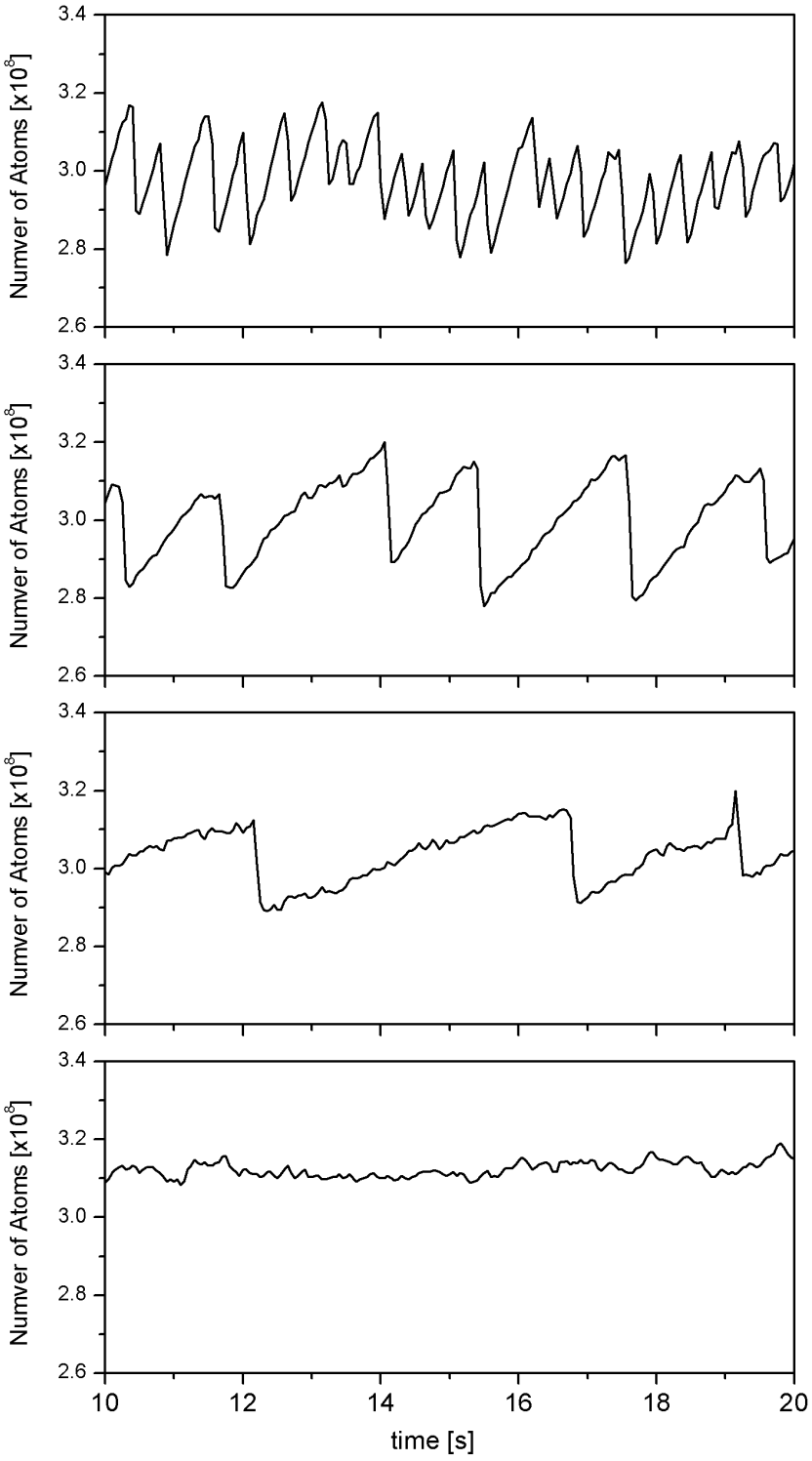

Figure 5.14: *Ten second interval from the loading curve of the 3D-MOT showing the unstable behavior of the 3D-MOT for four different laser detuning of the 3D-MOT trapping beams. The difference in laser detuning is about 0.4 MHz. From bottom to top the laser detuning is respectively 7.8 , 8.2 , 8.5 and 9.0 MHz.*

Chapter 6

New type of compact ultra cold Rb^+ ion-source

6.1 Introduction

High-brightness ion beams find applications in many areas of science and technology, including advanced high energy accelerators, ion beam microscopy, microelectronics and materials processing [7]. For instance, they are used in FIB (Focused Ion Beam) applications [24]. This technology enables localized milling and deposition of conductors and insulators with high precision (see Figure 6.1). The parameter that is used to quantify the source quality is the transverse reduced brightness B_r, i.e. the current density per unit of solid angle and per unit of beam energy. The brightness is defined as

$$B_r = \frac{\partial^2 I}{\partial A \partial \Omega \, U}, \tag{6.1}$$

where I is the beam current, A the source area, Ω the solid angle which the ions are emitted and U the longitudinal beam energy. Another way of expressing the transverse reduced brightness in terms of beam temperature T, ion flux Φ_{ion} and beam area A is

$$B_r = \frac{e^2 \Phi_{\text{ion}}}{\pi A k_B T} \tag{6.2}$$

where k_B is Boltzmann's constant and e the elementary charge. This is a valid approach for a thermal source with temperature T

Todays state-of-the-art ion beams come from Liquid Metal Ion (LMI) sources and produces ion beams with a reduced brightness up to 10^6 A/sr m^2V [7]. This is achieved by starting with a very small source area A, i.e. a few nanometer, while the the source temperature T is very high, typically 5000 K. These sources are also called field emission sources. From Equation 6.1 one can see that the brightness can be increased by reducing the beam divergence Ω by reducing the source temperature T. This can also be achieved by using laser cooling of a atomic beam followed by photo-ionization as proposed by Freinkman *et al.* [8]. Such a cold atomic beam can also be produced from trapped atoms. In both cases the ions have temperatures in the $1mK$ range, compared

to the 10^4 K range for ion beams generated by field emission sources [25]. Bases on the ion source presented by Freinkman *et al* [8] we will develop a new high brightness ion source by also reducing the source area A. This will be achieved by using a Magneto-Optical Compressor (MOC).

In this chapter we will propose a compact Rb^+ ion source using laser cooling and magneto-optical compression of an atomic beam from a vapor cell oven. The concept and theory are illustrated more in detail in the next sections. Also a simulation model to calculate the reduced brightness B_r is presented. Results show that this new ion source concept can lead to very high brightness for the ion beam. These results are presented in the following sections.

Figure 6.1: *Picture of a typical Focused Ion Beam (FIB) system. This system is a FEI Company Nova600 DualBeam in which also a scanning electron microscope is incorporated.*

6.2 The concept of the new ion source

In this section we will present the concept of the cold Rb^+ ion source. We propose the setup shown in Figure 6.2, which consists mainly out of three parts. The first part of the setup is a (recirculating) oven containing rubidium vapor, a so-called Knudsen cell, maintained at the desired temperature. The rubidium atoms leave the oven chamber through an aperture D_1 and enter a second chamber where they are collimated to a beam by a second aperture D_2, at a distance ℓ of the source. The aim of the second aperture D_2 is to filter all the atoms that will not be cooled and trapped in the next part of the setup. In order to keep things not to complicated we will assume $D_{1,2} = D$. Furthermore we will define the opening angle $\Delta\theta = \tan(D/\ell)$. The collimated beam then enters the second part of the setup. In this chamber the atomic beam is cooled and compressed in the transversal direction using a magneto-optical compressor. The cooling will reduce the transversal velocities to the Doppler cooling limit (see Section 2.2) and the trapping step will reduce the area of the cold beam by a factor of 10-100. The second part can also be used without the trapping step, i.e. the temperature T of the beam is reduced but not the beam area A, which was the proposed ion source by Freinkman *et al.* [8]. At the end of the second part, a laser cooled and compressed atomic beam is delivered. In the third part this beam is photo-ionized by a laser. This results in a Rb^+-ion beam with very high brightness.

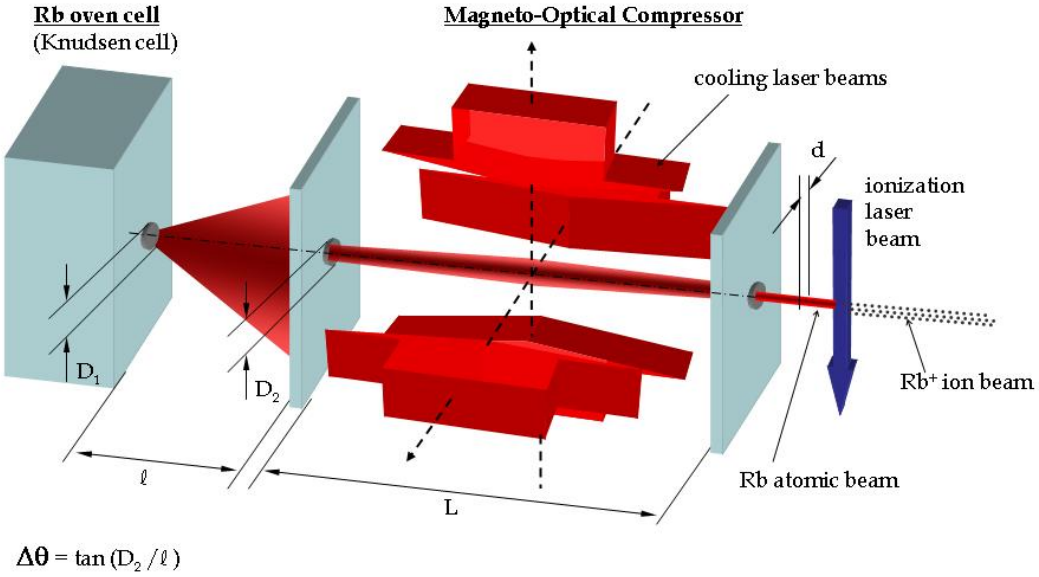

Figure 6.2: *Here the new Rb^+ ion-source is shown schematically. It mainly consist out of three parts: the first part is a vapor cell oven with double aperture to produce an atomic beam, the second part is a 2D Magneto-Optical Compressor that produces a ultra cold atomic beam, and in the third part this beam is ionized to produce a continuous high brightness ion beam.*

6.2.1 Estimate of performance

We will now do a simple estimate of performance for this new type of ion source. We start with the first part of the setup, the oven chamber. From the thermodynamics and theory of effusive sources explained more in detail in Section 6.3, we estimate the total flux Φ_0 that will leave the orifice as

$$\Phi_0 = \frac{1}{4} n A \sqrt{\frac{8 k_B T_s}{\pi m}}, \tag{6.3}$$

where T_s is the source temperature, n the density of atoms inside the source, A the area of the orifice and m the atom's mass. In order to cool the atoms to the Doppler temperature (Equation 2.10), the angle $\Delta\theta$ must be chosen $\Delta\theta \approx v_{cap}/\langle v \rangle$, where v_{cap} is the capture velocity and $\langle v \rangle$ the thermal velocity related to the source temperature. After the second aperture, that we will choose equal to the source aperture, the atomic beam is collimated and the resulting flux is

$$\Phi_1 \simeq \Phi_0 (\Delta\theta)^2. \tag{6.4}$$

Without laser cooling or trapping the resulting reduced brightness of the atomic beam, as introduced in the introduction of this chapter, is

$$B_{\text{initial}} = \frac{\Phi_1}{\pi A k_B T_i}, \tag{6.5}$$

where $T_i \simeq m v_{cap}^2 (\Delta\theta)^2 / 2 k_B$ is the initial temperature of the collimated beam. By cooling this atomic beam to the Doppler temperature T_D in transverse direction an increase in brightness will be obtained. This increase in brightness can be calculated as

$$B_c = B_i \frac{T_i}{T_D}. \tag{6.6}$$

From this equation it is clear that reducing the temperature of the beam with some factor will result in a brightness increase of the same order.

In addition, with magneto-optical compression it is also possible to decrease the beam area A and thus to increase the atomic beam brightness even more. Here the length available for compression L plays an important role. It determines the compression time $t = L/\langle v \rangle$. Together with the maximum acceleration that can be obtained with laser cooling and trapping, $a_{\max} = h\gamma/8\lambda m$ (Section 2.4), an initial area $A_i = \pi r_i^2$ can be compressed into a final area $A_f = \pi k T_D / \kappa$, where $\kappa = k \mu_B s_0 \nabla B$ is the spring constant as given in Section 2.4. The initial radius can be calculated as $r_i = a_{\max} t^2/4$. With magneto-optical compression the reduced brightness B_{ct} of the atomic beam is given by

$$B_{ct} = \frac{(1/4) n \langle v \rangle (\Delta\theta)^2 \kappa r_i^2}{\pi (k T_D)^2} \tag{6.7}$$

$$= B_i \left(\frac{T_i}{T_D}\right)\left(\frac{A_i}{A_f}\right). \tag{6.8}$$

Finally, the resulting reduced ion beam brightness is $B_r = e^2 B_{ct}$, with a current $J = e\Phi_1$ if we assume that we can make an ion out of every atom by photo-ionization.

6.2.2 Plugging in some numbers

Plugging realistic numbers for ^{85}Rb into these equations gives the potential performance of such a cold *Rb*-source for ion beam applications. The vapor pressure of Rubidium at a temperature T inside a oven chamber is given by an Antoine equation [21]

$$p_{\text{sat}} = p_0 e^{-T_0/T}. \tag{6.9}$$

where $p_0 = 1.1 \times 10^3$ Pa and $T_0 = 4040$ K for *Rb*. Using the theory of ideal gasses the density of Rb particles inside the oven chamber can be determined with

$$n = \frac{p_{\text{sat}}}{k_b T}. \tag{6.10}$$

In Figure 6.3 the left plot shows the vapor pressure for Rb inside the oven chamber and the right plot shows the density number of Rb atoms, both versus oven chamber temperature. The numbers we used to estimate the ion beam performance are given in Table 6.1. Plugging in these numbers into Equation 6.2.1 results in an atomic beam

Table 6.1: *The numbers used in the estimate of performance of the new ion source. The laser cooling and trapping parameters are found in [11]*

n	6×10^{18} m^{-3}	T_s	100^oC
$\langle v \rangle$	300 m/s	v_{cap}	4.7 m/s
T_D	144 μK	m	1.4×10^{-25} kg
$\Delta\theta$	10 mrad	L	5 cm
t	140 μs	r_i	500 μm
I	33 W/cm^2 ($2\times I_0$)	∇B	0.8 T/m

brightness of B_{ct}=2.8×10^{47} /m^{2}radJs for a magnetic field gradient of 0.8 T/m and $B_{ct} = 2.8 \times 10^{47}$ /m^{2}radJs if we apply NO gradient. Translating this into a reduced ion beam brightness

$$B_r = 3.2 \times 10^9 \text{ A/m}^2\text{srV} \ @ \ J = 1.8 \times 10^{-9} \text{ A } (\nabla B\text{=}0.8 \text{ T/m})$$

and respectively

$$B_r = 2.0 \times 10^5 \text{ A/m}^2\text{srV} \ @ \ J = 1.8 \times 10^{-9} \text{ A } (\nabla B\text{=}0)$$

If we compare this to the reduced brightness to a state-of-the-art LMI source, where $B_r \approx 10^6$ A/sr m^{2}V at a current J=10 pA [1], we conclude that the concept of the new ion source is very promising.

From these calculations we can conclude that this new type of ion source is very promising. In the next sections we will study the potential performance of such an ion source more in detail. First we will introduce some thermodynamics and theory related to the setup. Then a computer program is presented that will simulate atoms in a magneto-optical compressor. The results of this study are presented in the section Results. Finally we will give some conclusions and outlook concerning this new concept for an ion source.

[1] Also higher currents up to 1 μA can be obtained for the LMI source but this at a lower brightness.

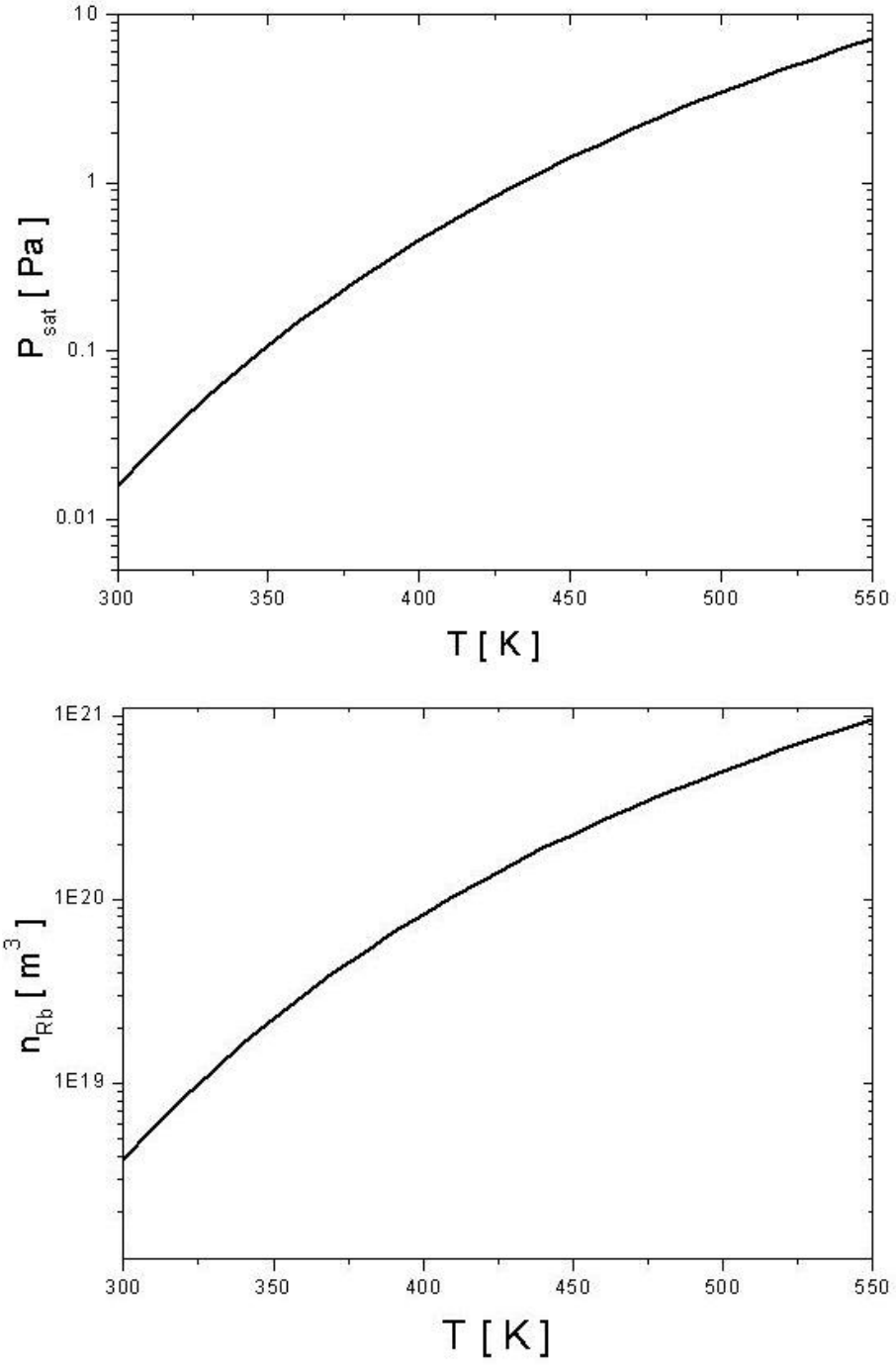

Figure 6.3: *Rubidium vapor pressure and rubidium density as function of temperature.*

6.3 Kinetic Theory of Effusive Sources

In this section some essential thermodynamic properties are presented. The aim is to introduce some additional physics concepts that will help to understand the principles behind the new ultra cold Rb^+ ion-source presented in this chapter.

6.3.1 Maxwell-Boltzmann distribution

The motion of atoms and molecules in a gas can be described using statistical mechanics [19]. From this theory the Boltzmann energy distribution, $P(E) \propto \exp(-E/k_BT)$, can be derived, where E is the total energy of a particle and $P(E)$ is the probability distribution as function of energy for a thermal system. Here the term $\exp(-E/k_BT)$ is known as the Boltzmann factor. The energy of free atoms is than given by $E = mv^2/2$ where $\mathbf{v} = (v_x, v_y, v_z)$ is the atomic velocity and $v = |\mathbf{v}|$ is the atomic speed.
The fraction of atoms $f(v)dv$ traveling with speeds between v and $v + dv$ is given by

$$f(v)dv = \frac{4}{\sqrt{\pi}}(\frac{m}{k_BT})^{3/2}v^2e^{-mv^2/2k_BT}dv, \tag{6.11}$$

where the prefactor can be obtained by normalization. This speed distribution function is known as the **Maxwell-Boltzmann speed distribution**.
An important value from the Maxwell-Boltzmann is the mean velocity $\langle v \rangle$ which is given by

$$\langle v \rangle \quad = \quad \int_0^\infty vf(v)dv = \sqrt{\frac{8k_BT}{\pi m}}. \tag{6.12}$$

6.3.2 Effusive sources

Effusive atomic and molecular sources with a thin-walled orifice are simple and compact and can be used for practically all molecules and most atoms. Because the orifice is small compared with the total area of the walls of the source, the thermal equilibrium of the gas inside is not disturbed by the effusing particles. Therefore, the effusion rate as well as the angular and velocity distribution of the particles exiting from such an orifice can be calculated from the kinetic gas theory as given in the previous section. In this treatment the free mean path, Λ, in the source is assumed large compared with the diameter of the orifice. This means that collisions do not occur inside the beam. The mean free path expressed in terms of density n is given by [19]

$$\Lambda = \frac{1}{\sqrt{2}n\sigma} \tag{6.13}$$

with the collision cross-section of the particles $\sigma = 1.7 \times 10^{-17}$ m^2 [22]. At a Rb oven temperature $T = 373$ K, which corresponds to a vapor density of $n = 6.20 \times 10^{18}$ atoms/m^{-3}, the mean free path is $\Lambda \approx 8 \times 10^{-3}$ m, which is larger than the 1 mm diameter of the orifice.
The number of atoms or molecules, dN, leaving the orifice erea element, dA, during

the time interval, dt, with a velocity between v and $v + dv$ into a solid angle element, $d\Omega = \sin\theta \, d\theta \, d\phi$, is given by [20]

$$dN = nvf(v)dv\frac{d\Omega}{4\pi}\cos(\theta)\, A\, dt. \tag{6.14}$$

Integrating the velocity distribution over all θ and v results in the total flux $dN/dt = \Phi$, given by the familiar expression

$$\Phi = \frac{1}{4}nA\langle v\rangle. \tag{6.15}$$

6.4 Simulation Model for the MOC

In Section 6.2 we estimated the ion beam performance of the new ion source. There we assumed that all particles had a velocity equal to the average velocity. In a real atomic gas the velocity has a Maxwell-Boltzmann distribution. This leads to a far more complicated distribution then the in the estimate in Section 6.2. Therefore it is necessary to simulate the particle trajectories in our new ion source for the Maxwell-Boltzmann distribution.

In this section we will introduce the computer program that is used to simulate the performance of the new ion source. The computer program simulates the particle trajectories in the second part of the setup, i.e. the 2D Magneto-Optical Compressor (MOC). The output of the simulation is a particle distribution that can be translated into the final ion beam distribution by weighting it with the corresponding initial particle distribution. From these results the performance of the ion source (brightness, emittance, current, etc.) is calculated and compared with the numbers estimated in the previous section. The simulation program is written using Matlab software and the code is given in the Appendix.

There are some assumptions we did in the model used for the simulations. First in a real setup there is a very complicated symmetry. We simplify the symmetry by assuming a quasi-circular symmetry. We perform a 1D-simulation and weighting it with the initial particle distribution that we consider circularly symmetric. Furthermore only deterministic forces are taken into account, neglecting spontaneous emission forces. Therefore the final temperature of the particles can be lower than the Doppler temperature ($T < T_D$). This is checked manually and we will not present any results where the final temperature of the beam is lower than the Doppler temperature.

6.4.1 Initial particle distribution

First we take a closer look at the initial particle distribution that is used as input for the simulations. The program generates an initial particle distribution given a velocity range $[0, v_{\max}]$ and a maximum angle $\theta_{\max} = D/\ell$ where D is the source diameter and ℓ is the length between the source and the MOC. By estimating the maximum radius the atoms can start from to have enough time to reach the center of the beam within a realistic interaction length $L = 5$ cm ($r_{\max} \approx a_{\max} L^2/\langle v_z \rangle^2 = 550\mu$m), we have chosen the the diameter of the source aperture $D = 1$ mm. If $N_v = v_{\max}/\Delta v + 1$ is the number of velocity steps and $N_\theta = 2\theta_{\max}/\Delta\theta + 1$ the number of angle steps, $\xi = N_v \times N_\theta$ is the total number of grid points for each point source. The third variable is the number of point sources, N_s, used to model a source aperture. The initial particle distribution is constructed in three steps:

1. First a distribution is constructed for a single point-source on the z-axis based on Equation 6.14 in spherical coordinates,

$$P(v_i, \theta_j) = A\, v_i^3 e^{-Bv_i^2} \cos(\theta_j) \tag{6.16}$$

for all i and j, where i and j are respectively the index of the velocity- and angle-number. This distribution is used to weight the results of the simulation to calculate the final ion beam distribution.

2. This spherical coordinates (v, θ) are then transformed into cylindrical coordinates (r, v_r, v_z) using $v_r = v_i \sin(\theta_j)$,$v_r = v_i \cos(\theta_j)$ and $r_{ij} = \ell \tan(\theta_j)$ where ℓ is the distance between source and aperture.

3. In the third step the initial distribution for a finite source aperture is simulated by adding up a series of point-sources to construct the total initial distribution $P_{\text{tot}}(r, v_r, v_z)$

$$P_{\text{tot}}(r, v_r, v_z) = \sum_{k=1}^{N_s} P_k(\sqrt{v_r^2 + v_z^2}, \text{atan}(\frac{r_{kj} - r_k}{\ell})) \tag{6.17}$$

where $r_{kj} = r_k + \ell \tan(\theta_j)$, r_k the distance from the center of the aperture to the k^{th} pointsource and N_s is the number of point sources (see Figure 6.4). Only the particles between the aperture range $[-D_2/2 < r < D_2/2]$ are taking into account.

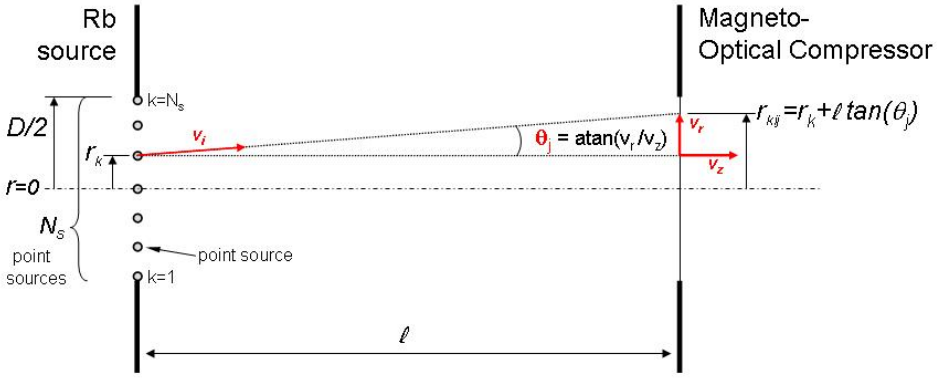

Figure 6.4: *Schematic overview of the geometry of the point sources.*

6.4.2 Magneto-Optical forces

For every particle of the initial distribution the Newtonian equation $\mathbf{F} = m\ddot{\mathbf{x}}$ is solved over the distance inside the MOC. At the end of the MOC we end up with new coordinates (r', v_r', v_z') for all particles of the initial beam distribution. The forces applied during the MOC phase are calculated from (see Section 2.3)

$$F(x) = F_+(x) + F_-(x) \tag{6.18}$$

$$F_\pm(x) = \pm \frac{\hbar k \Gamma}{2} \frac{s_0}{1 + s_0 + 4(\Delta_{x\pm}/\Gamma)^2} \tag{6.19}$$

where as in Section 2.3

$$\Delta_{x\pm} = \delta \mp kv \mp \mu_B \nabla B_x x/\hbar \tag{6.20}$$

is the effective frequency detuning of the laser field, k the wave vector, Γ the atomic linewidth, s_0 the saturation parameter and ∇B_x is the gradient of the magnetic field along the x-axis. For the simulations presented in this work the saturation parameter will be varied between $0.5 < s_0 < 2$, the detuning $-0.5\Gamma < \delta < -1.5\Gamma$ and the magnetic field gradient $0 < \nabla B < 2$ T/m.

In Figure 6.5 the molasses force (Equation 6.18 for x=0) from the simulation model is plotted for rubidium atoms and for a detuning of $\delta = -\Gamma$. In the graph the dotted lines represent the molasses force produced by each separate laser beam. We can see that these forces have a Lorentzian line shape. Most important from this graph is that we can see that the capture velocity v_{cap} is around 5 m/s. This corresponds well with the theoretical value which can be estimated by $v_{cap} = \Gamma/k = 4.7m/s$ [11]. In Figure 6.5 the compression force (Equation 6.18 for v=0) is plotted as function of position for constant velocity for a detuning of $-\Gamma$ and a magnetic field gradient of 0.5 T/m. This force has the same shape as the cooling force and will accelerate the atoms to the axis. From this graph we can see that the capture range is around 1 mm. Also this fits well with the theoretical value expected by $x_{cap} = \hbar\delta/\mu_B \nabla B = 8 \times 10^{-4}$ m (See Section 2.3).

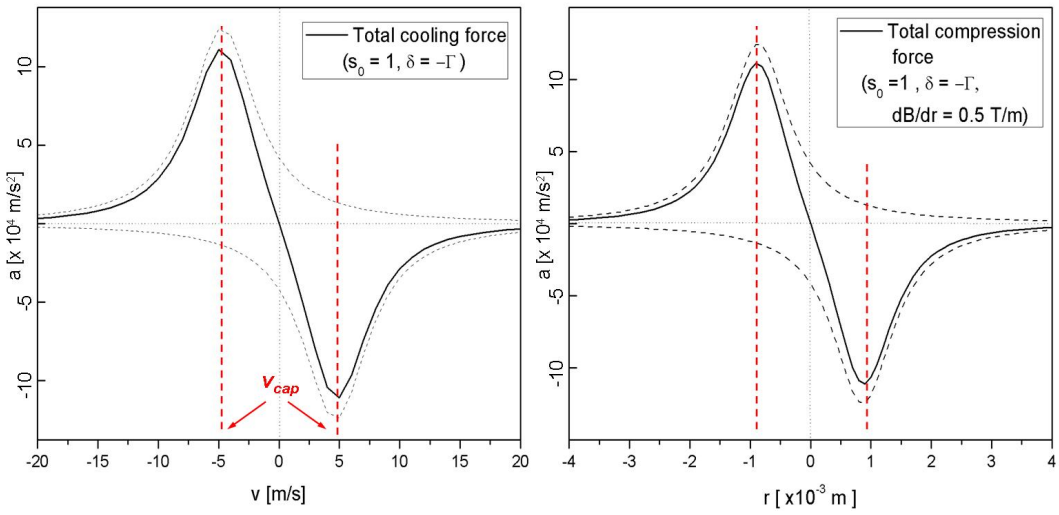

Figure 6.5: *The left graph shows the cooling force (Equation 6.18 as function of velocity and x=0. From the red dotted vertical lines we see that the capture velocity v_{cap} is around $4.7m/s$ for $\delta = -\Gamma$. The bold line is the total force, the dotted lines represent the separate force of each laser beam. The right graph shows the compression force as function of the position from the axis and for v=0. Here we see that the capture range x_{cap} is around 1×10^{-3} m for $\delta = -\Gamma$ and $\nabla B = \Gamma/2m$.*

6.4.3 Photo-ionization of the atomic beam

As output from the magneto-optical compressor we have neutral Rb atoms. The aim was to develop an ion source, so the Rb atoms have to be transformed into Rb^+-ions. This is possible by photo-ionization. This is a two step procedure (see Figure 6.6). First the Rb atoms have to be excited, ($5S_{1/2}(F=3) \rightarrow 5P_{3/2}(F=4)$) with a laser at a wavelength of 780 nm. If the Rb atoms are in the excited state, they can be ionized with a 480 nm laser [23], which is a crucial step. The intensity needed to ionize all the atoms in the excited state is equal to $P \approx \pi dv\hbar\omega/4\sigma$, where $d \approx 0.1mm$ is the diameter of the atomic beam, $v \approx 300m/s$ the forward velocity of the atoms, $\hbar\omega = 3eV$ the energy of one photon and $\sigma = 1.48 \times 10^{-21}m^{-2}$ [28] the photo-ionization cross section of Rb. Using the given numbers we find that the total photo-ionization power is around $P \approx 8W$ which means that with the current laser we would need a cavity.

Taking into account this power we assumed for all the reduced brightness calculations that we are able to turn every atom into an ion. So $B_r = e^2 B_r^{\text{atoms}}$.

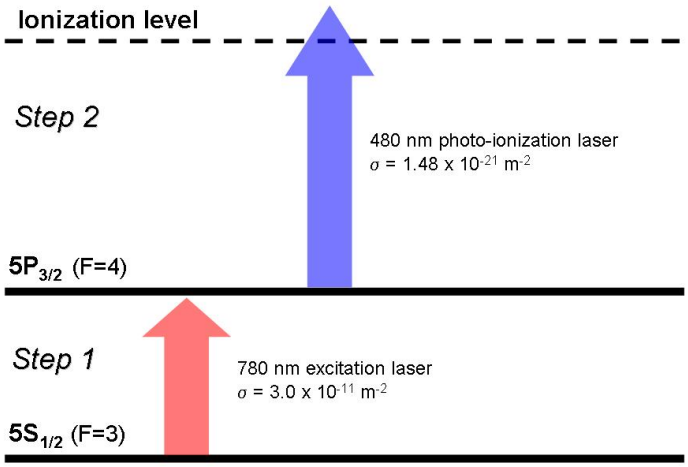

Figure 6.6: *Ionization scheme: Two step proces to photo-ionize Rb atoms. First the Rb atoms have to be excited from* $5S_{1/2}(F=3) \rightarrow 5P_{3/2}(F=4)$ *with a laser at a wavelength of 780 nm. In the second step a a 480 nm laser will photo-ionize the atoms to create the ions. The absorbtion cross-section are given by* σ.

6.4.4 Beam characteristics

From the final beam distributions some characteristic numbers are calculated to determine the beam quality and ion-source performance. As mentioned in the introduction, the reduced brightness, Equation 6.1, is the most important parameter that quantifies

the beam quality. The reduced brightness of the ion beam is calculated as

$$B_r = \frac{1/4\, nA\langle v\rangle(\Delta\theta)^2}{4\pi^2 m\epsilon^2}e^2, \tag{6.21}$$

where $A = \pi d^2/4$ the area of the source aperture and ϵ the root-mean-square emittance calculated as

$$\epsilon = \sqrt{\langle r^2\rangle\langle v_r^2\rangle - \langle r v_r\rangle^2}. \tag{6.22}$$

The rms values are calculated using

$$\langle r^2\rangle = \frac{1}{N}\sum_{i=1}^{N_g} r_i^2 P_{\rm tot}(r, v_r, v_z), \tag{6.23}$$

$$\langle v_r^2\rangle = \frac{1}{N}\sum_{i=1}^{N_g} v_{r,i}^2 P_{\rm tot}(r, v_r, v_z), \tag{6.24}$$

$$\langle r v_r\rangle = \frac{1}{N}\sum_{i=1}^{N_g} r_i v_{r,i} P_{\rm tot}(r, v_r, v_z), \tag{6.25}$$

where $N = \sum_{i=1}^{n} P_i(r, v_r, v_z)$ is the total number of particles taking into account during the simulation and $N_g = N_v \times N_\theta \times N_s$ is the number of grid points.

6.4.5 Beam fraction and peak brightness

The simulation program calculates a final beam distribution given an initial beam distribution and magneto-optical forces acting over a given interaction length. From that final beam distribution all the important beam parameters, that characterize the beam quality, such as root-mean-square (rms) transversal velocity and beam size are calculated as function of the beam fraction. This beam fraction is the fraction of total flux within a given area πr^2 where r is the radius of the final beam. Physically it means that an aperture is placed in the beam with area πr^2. A typical example of the reduced brightness B_r as function of beam fraction f for both laser collimation and magneto-optical compression is the first graph shown in the Section Results (See Figure 6.7).
For the results in the following section we will characterizing the beam quality by giving only one number, the reduced peak brightness B_r^p, that is the reduced brightness for a beam fraction f near zero

$$B_r^p = \lim_{f\to 0} B_r(f). \tag{6.26}$$

6.5 Results

6.5.1 General remarks

In this section we present and discuss some of the results derived from the simulations of the new ultra cold ^{85}Rb ion source. The section is divided into two subsections. In the first subsection we present the results from the laser collimation, i.e. the laser cooling of the atomic beam, and the second subsection we also deal with magneto-optical compression of the atomic beam.
But first we start to simulate the particle trajectories in the MOC using the same parameters as we used for the estimate of performance in Section 2.2. We summarized the parameters used in Table 6.2 and the results from the simulation are shown in Figure 6.7. Here we see the reduced brightness as function of beam fraction for the two cases as calculated in Section 2.2. There are two important observations is we compare the cases for laser collimation and laser compression. (1) For the laser collimation the brightness is constant for the most part of the beam fraction, which means that reducing the beam fraction will only lead to a decrease in beam current but will not result in a higher brightness. This can be explained by studying the temperature of the beam as function of beam fraction. The uniform temperature profile of the beam will result in an uniform brightness profile as observed. (2) By adding magneto-optical compression the beam brightness becomes strongly dependent from the beam fraction. Using only a small fraction of beam results in a smaller current but the beam brightness increases by orders of magnitude. Again this can be explained by considering the density of the beam. This last one is not uniform anymore and is higher towards the axis where the temperature will be the lowest. Finally the horizontal dotted lines in the graph represent the estimated ion beam brightness from section 6.2. We can see that for the laser collimation the estimate and simulation result match well. For the case with a magnetic field gradient of 0.8 T/m the simulation shows that the reduced brightness is lower than the estimated value. This is due to the complexity of both our initial particle distribution and MOC-forces. From these first results we can conclude that our first estimate was accurate for the laser collimation but we will have to be careful when considering compression forces.

Table 6.2: *The numbers used in the simulation of the new ion source. These are the same numbers as in Table 6.1 where we estimated the performance by simple equations.*

n	6×10^{18} m^{-3}	T_s	100^oC
$\langle v \rangle$	300 m/s	v_c	4.7 m/s
T_D	144 μK	m	$1.4{\times}10^{-25}$ kg
$\Delta\theta$	10 mrad	L	5 cm
∇B	0.8 T/m	r_i	500 μm

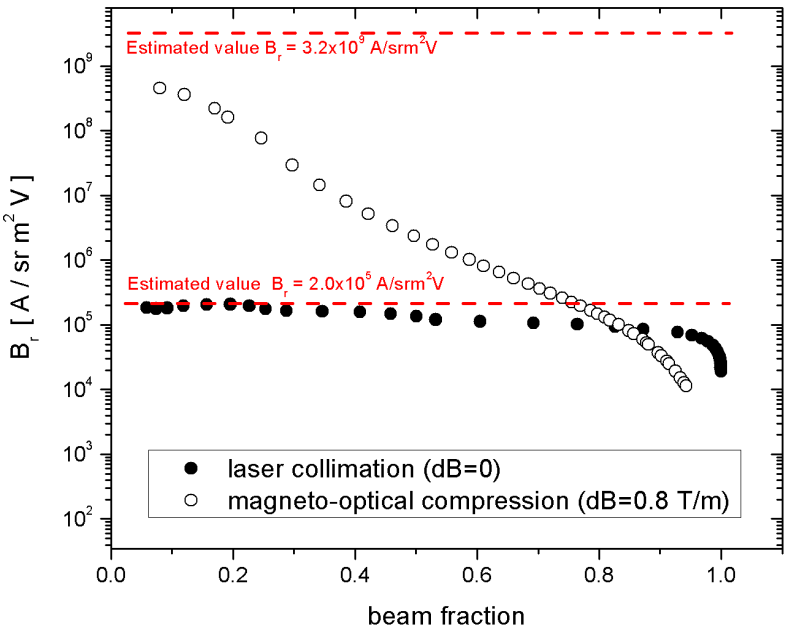

Figure 6.7: *The reduced brightness as function of beam fraction. This is a typical example of the data obtained with the simulation. In the next chapters the beam performance will be expressed in reduced peak brightness, defined as the reduced brightness for a beam fraction approaching to zero.*

6.5.2 Laser collimation

In this section we will study the final reduced peak beam brightness for different parameters of the source. These parameters can be related to the rubidium source itself, such as source temperature T_s or opening angle $\Delta\theta$, or to the laser collimation and compression parameters such as saturation parameter s_0, interaction length L, laser detuning δ or magnetic field gradient ∇B. In this section we will only study laser collimation of the beam, i.e. for $\nabla B = 0$. In Subsection 6.5.3 the magneto-optical compression will be added. This study should give us a clear view of the important parameters to consider when designing this new type of source.

Opening angle

The opening angle $\Delta\theta = \tan(D/\ell)$ is defined as the maximum angular spread for the atomic flux from the source. This angle fixes the ratio between the diameter for the source D and the distance between source and the 2D magneto-optical compressor ℓ. It limits the average transverse velocity of the beam by $v_r = \langle v \rangle \Delta\theta$. If v_r becomes larger then v_c, it is not possible anymore to estimate the ion beam performances easily using only the simple equations. For these circumstances, i.e. for $\Delta\theta > v_c/\langle v \rangle$, simulations can help us to understand the behavior. Therefore simulations where done for different opening angles $\Delta\theta$. The diameter of the source D was maintained constant. The variation in opening angle was done by varying the length ℓ between source and magneto-optical compressor. The resulting brightness of the beam as function of opening angle is given in Figure 6.8. In the plot two different behaviors are observed.

The left part of the graph, $\Delta\theta < 25$ mrad, shows a constant reduced peak brightness as function of opening angle. If we consider Equation (6.2.1) and study the dependence of opening angle we can observe the following : (1) By increasing $\Delta\theta$ we see that the brightness increases quadratically, i.e. $B_r \propto (\Delta\theta)^2$. (2) The final temperature of the beam increases quadratically and the brightness goes as $B_r \propto 1/T^2$. We can derive the last proportionality for Equation 6.21 using $v_0 = \langle v \rangle \Delta\theta$ and $T \propto v^2$. If we take into account both considerations we find that the reduced brightness as function of opening angle is constant. This is shown with the horizontal dotted line in Figure 6.8

As we can see in the Figure 2.2 the cooling force decreases for atoms with a transverse velocity higher than the capture velocity v_c. At a detuning of $-\Gamma$ this force decreases significantly for velocities above 8 m/s ($\approx 2 \times v_c$). This corresponds to an opening angle around 26 mrad. In Figure 6.8 we can see that the reduced brightness decreases as well for $\Delta\theta > 25$ mrad. This can be explained by the higher final temperature of the beam because laser cooling is not efficient anymore above $\Delta\theta > 26$ mrad. From this study we can conclude that the choice of opening angle is not important in terms of brightness as long as this opening angle stays below $\Delta\theta < 2v_c/\langle v \rangle$. In the further simulations the opening angle will be set at a constant value of 10 mrad to neglect this effect.

Laser detuning

Another important laser cooling parameter is the laser detuning. The laser detuning δ, mostly expressed in terms of the line width Γ, is the difference between laser frequency and atomic resonance frequency. The laser detuning is one of the parameters that de-

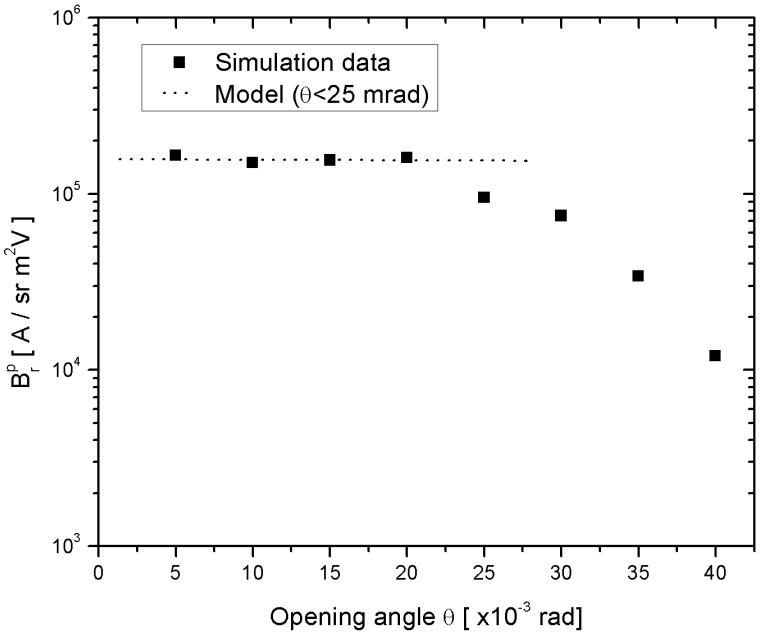

Figure 6.8: *Simulation results for the reduced brightness as function of the opening angle. The dotted line represents the fit using the model B_r = constant for $\Delta\theta < 25$ mrad.*

termine the damping coefficient α (see Equation 2.7). In Figure 6.9 simulations of the reduced peak brightness for an ion source are given as function of laser detuning δ.
To understand this behavior, we used $B_r \propto 1/v_r^2$ and the damping coefficient dependency on velocity v in Equation 2.9 to fit the data obtained by the simulations. The dotted line in Figure 6.9 represents the fit using

$$\ln(B_r) \propto \frac{\delta/\Gamma}{(1 + s_0 + 4(\delta/\Gamma)^2)^2}. \tag{6.27}$$

We see that with this model it is possible to accurately predict the laser detuning dependency of our new ion source.
At a detuning $\delta = 0$ no net laser cooling force is present. The reduced peak brightness at this point is the initial brightness of the system without additional laser collimation and can therefore be seen as a reference value. From these results we can conclude that the optimal detuning is around $\delta = -\Gamma/2$. We can validate this number by checking that the damping coefficient has a maximum there ($\partial\alpha/\partial\delta = 0$), which is indeed the case. This detuning will therefore be used for further simulations in this work.

Saturation parameter

The saturation parameter $s_0 = I/I_0$ indicates the laser intensity I as a ratio of the saturation intensity I_0 of the atoms. For the case of low saturation, $s \ll 1$, the population of atoms is mostly in the ground state, whereas in the case of high s_0, the population is equally distributed between ground state and excited state. In terms of design of the new source it indicates how much laser power is needed to operate the system. But

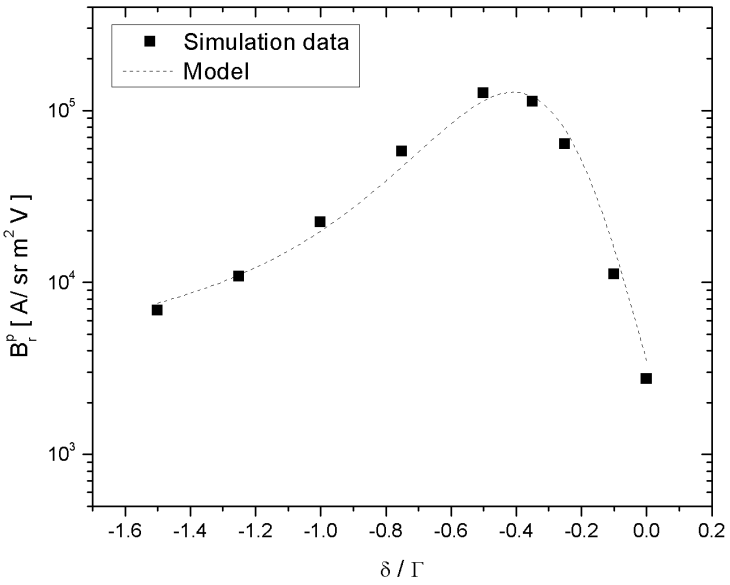

Figure 6.9: *Simulation results for the reduced brightness as function of the laser detuning.*

most important, the saturation parameter used will also influence the performance of the resulting ion beam, i.e. the reduced peak brightness.

Figure 6.10 shows the reduced brightness as function of saturation parameter for laser collimation. The dotted line in the graph shows the function

$$\ln(B_r) \propto \frac{s_0}{(1 + s_0 + (2\frac{\delta}{\Gamma})^2)^2}. \tag{6.28}$$

This model is derived the same way as the previous model for the laser detuning.
We can conclude that it will not help us to use a saturation parameter $s_0 \gg 1$ because the damping coefficient becomes smaller for $s_0 > 2$ at a detuning $\delta = -\Gamma/2$.

Interaction length

The interaction length L is the distance where atoms are interacting with the laser field and are cooled in the transverse direction. This interaction length is proportional to the time that atoms experience laser cool forces ($L \propto t$). In Figure 6.11 the reduced brightness from the resulting ion beam is plotted as function of interaction length.
From the plot we see that the peak brightness increases exponentially as function of interaction length. Again the dotted line in the graph shows the dependence of the interaction length L on the reduced brightness. The model we have used is constructed in the same way as the previous ones. Earlier we found that $B_r \propto \exp(2\alpha t/m)$. This time we can introduce the interaction length into this equation by using $t = L/\langle v_z \rangle$.

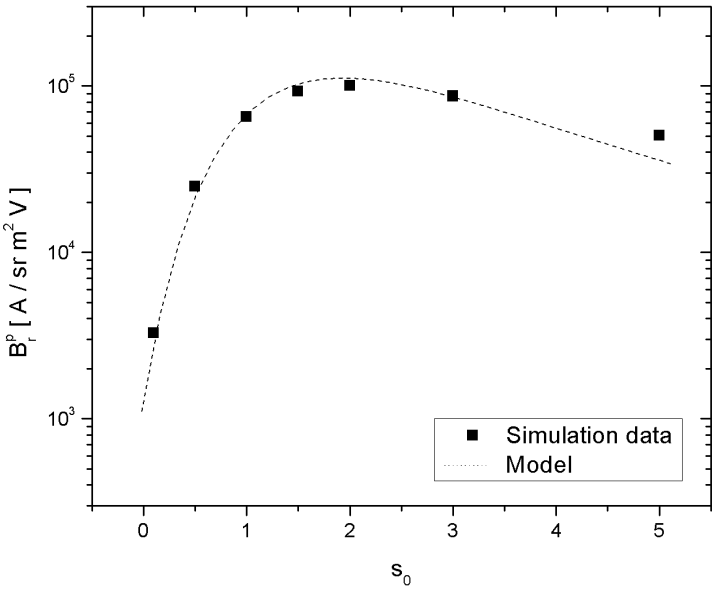

Figure 6.10: *Simulation results for the reduced brightness as function of saturation parameter s_0. The reduced brightness is normalized and the dotted line shows the model $ln(B_r) \propto s_0/(1 + s_0 + 2(\delta/\Gamma)^2)^2$.*

The model used to compare the data with is

$$\ln(B_r) \propto L. \tag{6.29}$$

This leads us to the conclusion that increasing the interaction length of the system will exponentially increase the brightness of the source until the final temperature of the beam reaches the Doppler temperature. Unfortunately this interaction length is limited by available laser optics and system dimensions. For the remaining simulations an interaction length of 5cm is used. This is a reasonable size for laser optics and final dimensions of the system.

Source Temperature

The temperature of the source is another important parameter. From Equation 6.1 we can see the parameters that influence the reduced beam brightness. In this equation the density of the atoms n, the average velocity $\langle v \rangle$, and both the final beam area A_f and temperature T_f depends on the source temperature T_s. The density of rubidium as function of source temperature is shown in the previous section in Figure 6.3. In Table 6.3 the density n, the vapor pressure p, atomic flux Φ_1 and average velocity $\langle v \rangle$ are given as function of source temperature for a ^{85}Rb source. Simulations for different source temperatures were done and results are shown in Figure 6.12. Here the reduced peak brightness is plotted as function of source temperature.

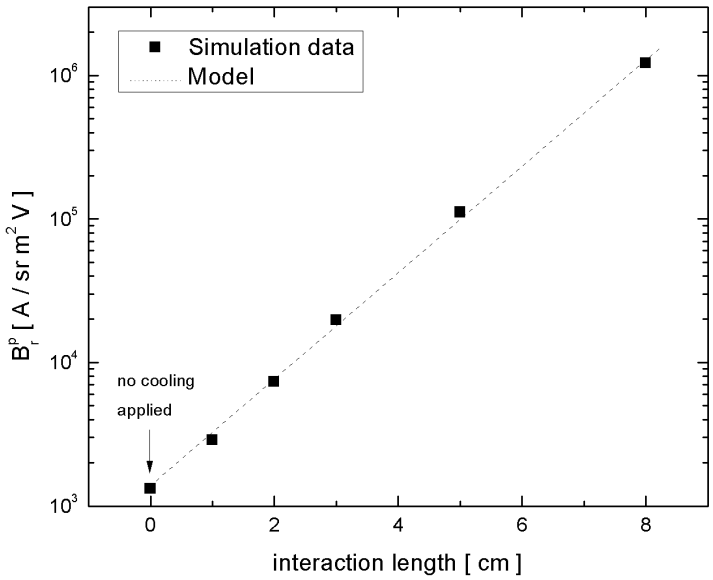

Figure 6.11: *Simulation results for reduced brightness as function of interaction length. The simulations where done for a saturation parameter of s_0=1, a detuning $\delta = -0.5\Gamma$, a source temperature of 100°C, opening angle of $\Delta\theta$=10mrad and no magnetic field.*

From Figure 6.12 we see that the brightness of the source increases by orders of magnitude for increasing temperature. By substituting Equation 6.10 and 6.12 into Equation 6.21 a model is derived for this behavior of the source temperature on the reduced brightness and is given by

$$B_r \propto \frac{1}{\sqrt{T_s}} e^{-\frac{4040}{T_s}}. \tag{6.30}$$

This model is used to fit the simulation data and is represented by the dotted line in the graph (See Figure 6.12). In this model only the dependence of density and average velocity on source temperature were taken into account. With these two dependencies we were able to fit the data very well. This leads to the conclusion that the increase in source temperature can boost up the brightness of the ion source by orders of magnitude mainly due to the density increase in the Rb oven. The velocity increase of the Rb atoms at higher source temperature leads to decreasing cooling performance, but this can be considered as a minor effect.

Although the reduced peak brightness keeps increasing with temperature, there are some limitations to keep in mind. First, above a temperature of 600 K the density of rubidium atoms becomes so high that they are likely to form molecules [26]. These molecules will not experience any laser cooling and trapping forces anymore. Secondly, as the density of the atomic beam reaches a certain limit, the atomic beam becomes optically dense and makes further cooling and trapping impossible. We will discuss this

effect later in the section on laser compression.

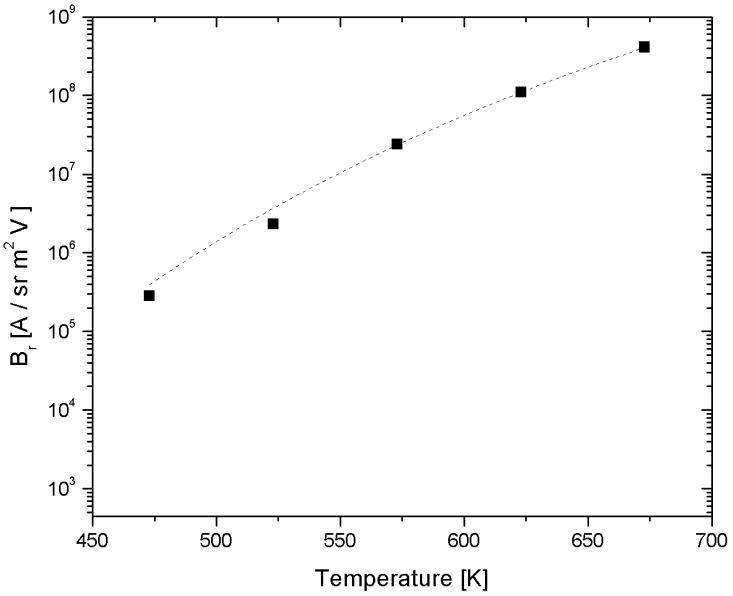

Figure 6.12: *Simulation results for reduced brightness as function of source temperature. The dotted line is the fit with the model* $ln(B_r) \propto T_s^{-1/2}\exp(-4040/T_s)$. *The other simulation parameters are given in Table 6.2*

Beam performances for laser collimation

We can conclude this laser collimation section by giving an overview of the most important parameters for the design of the new Rb^+ ion-source. Furthermore we can present the estimated beam properties and compare them with both the estimate made in Section 6.2 and the properties of the state-of-the-art LMI sources.
We found the optimal values for the laser detuning and saturation parameter of respec-

Table 6.3: *An overview of some important parameters as function of source temperature for a Rb oven. The atomic flux* $\Phi_0 = 1/4nA < v >$ *is calculated for a aperture of* $d = 1mm$, *and* $\Phi_1 = \Phi_0(\Delta\theta)^2$ *is the atomic flux inside the beam, where* $\Delta\theta = v_c/ < v >$.

$T_s[^oC]$	$p[mbar]$	$n[m^3]$	Φ_0 $[at/s]$	$\Phi_1[at/s]$	$< v > [m/s]$
100	2.64×10^{0}	6.20×10^{18}	3.76×10^{14}	9.70×10^{10}	309
150	4.54×10^{1}	1.01×10^{20}	6.52×10^{15}	1.48×10^{12}	329
200	4.43×10^{2}	9.22×10^{20}	6.30×10^{16}	1.28×10^{13}	348
250	2.25×10^{3}	5.46×10^{21}	3.92×10^{17}	7.24×10^{13}	366
300	1.24×10^{4}	2.35×10^{22}	1.77×10^{18}	2.98×10^{14}	383

tively $\delta = -\Gamma/2$ and $s_0 = 2$. The source temperature T_s was found to be an important parameter for the resulting beam brightness. The huge increase in brightness comes from the flux increase and results in a source with high brightness and high flux. In Table 6.5.2 the final beam properties for a source temperature of 100^{o}C and 300^{o}C are listed. Note that both the final beam size and temperature are very similar. This confirms that beam performance as function of source temperature is mostly driven by the increase in atomic flux which correspond exactly to the estimate in Section 6.2. If

$T_s[^o]C$	$B_r[A/srm^2V]$	$J_{tot}[A]$	$r_{rms}[m]$	$v_{rms}[m/s]$	$T_f[\mu K]$
100	2×10^5	1.5×10^{-9}	1.0×10^{-4}	0.13	150
300	3×10^8	1.3×10^{-5}	1.2×10^{-4}	0.15	225

we compare the performance of the new source, we can conclude that we are already competing to the state-of-the-art LMI source. Recently LMI ion source brightness up to 10^6 A/sr m^2 V, at currents of J=10 pA were reported. Already without applying magneto-optical compression it is therefore worthwhile to develop this new type of source.

6.5.3 Laser compression

In this section results are discussed for a source with magneto-optical compression. This is a combination of laser collimation and compression. Physically this means that a magnetic field gradient, perpendicular to the atomic beam axis, is added to the laser cooling system resulting in a reduction of the final beam area. Some important parameters as magnetic field gradient ∇B, laser detuning δ and interaction length L are studied to understand the performance.

Magnetic field gradient

By adding a magnetic field gradient perpendicular to the atomic beam axis, the scattering force will drive back the atoms to the atomic beam axis. This force is proportional to the distance from the axis, and the strength of the magnetic field gradient determines the spring constant. Compression of the beam will decrease the resulting beam area and from Equation 6.1 we see that this results in an increasing reduced brightness. A first estimate for this phenomenon was already made in the introduction.

Using the simulation model the reduced brightness was studied as function of magnetic field gradient. Results are shown in Figure 6.13. In the graph two different behaviors are observed. First, between zero and ∇B=0.8 T/m the reduced peak brightness increases exponentially with magnetic field gradient. This behavior can be modeled with the same model as previously, by studying the final beam radius. From Equation 6.1 $B_r \propto 1/\langle r^2 \rangle$, where now $r = r_0 \exp(-\mu_B t \nabla B/\hbar k)$ (See Equation 2.15). In Figure 6.13 the first part of the graph is compared with

$$\ln(B_r) \propto \nabla B. \tag{6.31}$$

This is shown with the dotted line.

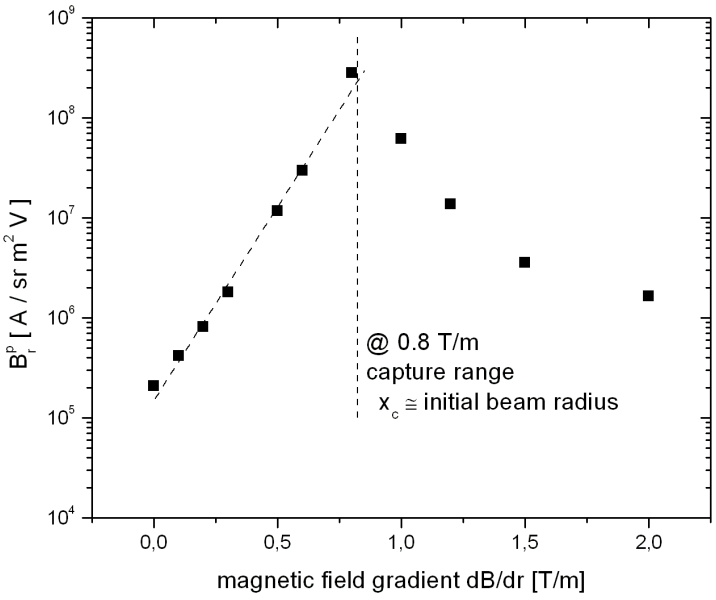

Figure 6.13: *Reduced peak brightness as function of magnetic field gradient. Settings as given in Table 6.2. The left dotted line is the fit through the data points using* $\ln(B_r) \propto \nabla B$. *The vertical line gives the magnetic field gradient where the capture range* x_c *equals the radius of the initial atomic beam* $r = D/2$.

We can conclude that increasing the magnetic gradient results into an exponential increase in reduced beam brightness up to a given point. In the second part of the graph, from ∇B=0.8 T/m up to 2 T/m, a decrease in reduced beam brightness is observed. Although this decrease is harder to quantify in a model, the explanation is found by studying the capture range r_c for different magnetic field gradient. Using the parameters from Table 6.2 and $\nabla B > 0.8T/m$, the capture range $r_c = \hbar\gamma/\mu_B\nabla B$ becomes smaller than the rms-beam size. Physically this means that the time to drive the atoms to the center exceeds the average time the atoms spend in the compressor ($\tau = L/\langle v_z \rangle$). We can conclude that the magnetic field gradient has to be chosen so that the capture range equals the average initial beam radius. The optimal magnetic field gradient ∇B is

$$\nabla B \approx \frac{2\hbar\gamma}{\mu_B D}. \tag{6.32}$$

Limitations for ultra dense atomic beams

Increasing the density of the beam leads to higher brightness. In the previous sections we saw that using a high source temperature and high magnetic field can help to improve the beam brightness. But there are some limits that have to be taken into account. At

high densities, when $nd\sigma > 1$, the atoms become optically thick and additional forces due to reabsorption of emitted photons leads to negative cooling effects [27]. Here σ is the effective collision cross section for light assisted collisions and d is the diameter of the beam. Typically this happens at densities around 10^{11} atoms/cm^3 for a beam diameter of 1 mm. At this density we can impose a simple condition in terms of atomic flux leading to

$$\frac{\Phi_1}{\pi r^2 \langle v_z \rangle} < 10^{17}[\text{atoms/m}^3] \tag{6.33}$$

where Φ is the atomic flux in atoms/s, r is the final radius of the beam and $\langle v_z \rangle$ is the average forward velocity.

6.6 Conclusions

We found that the strength of the magnetic field gradient is an important parameter to optimize the ion source. Without magneto-optical compression we found that we could produce an ion beam with reduced peak brightness up to 2×10^5 A/sr m^{2}V (at T_s=100^{o}C). With a magnetic field gradient of 0.8 T/m we could increase this reduced peak brightness up to $4{\times}10^8$ A/sr m^{2}V (at T_s=100^{o}C). For every magnetic field gradient there is a corresponding capture range r_c. Increasing the strength of the magnetic field gradient will only result in a higher brightness if the corresponding capture range is larger than the atomic beam radius.
Finally, we conclude so far that according to the first estimations and supported by our simulations outcome, the new ultra-cold Rb^+ ions source presented in this chapter is a very promising device. The performance exceeds that of LMI sources, which have a reduced brightness of 10^6 A/sr m^{2}V, by orders of magnitude.

6.7 Potential applications using different ion species

The new compact ultra-cold ion source presented in this thesis is based on cooling, trapping and ionizing Rb atoms. This because Rb is a common used atom that can easily be laser cooled, trapped and ionized. Although a detailed study has been done for Rb, this concept of new ion source can be extended towards different elements. The most important condition is that the atoms can be easily laser cooled, trapped and ionized. Potential elements are Lithium Li-7, Sodium Na-23, Potassium K-34 and Cesium Cs-133. We see that we could produce both light and heavy ions, depending on the application. To complete this work we studied the potential applications for this new compact ultra-cold ion source for two more elements, Li-7 a light element and Cs-133, that could produce heavy ions. Both elements could be interesting for different kind of applications.

6.7.1 Li^+ source for ion microcopy

A ultra-cold lithium ion source could be used as a source for a ion microscope as presented by B.W. Ward *et al.* [31] as an alternative for the Helium ion source used in this microscope. This microscope is built upon field ion microscope (FIM) technology. Here they use a cryogenically cooled metal needle witch has been sharpened to a radius around 100 nm. By placing this tip in a Helium vacuum background and applying a relative small voltage, helium ions in a spherical shape are generated to produce a focused spot size of 0.25 nm. This corresponds to a brightness $B > 4 \times 10^5$ A/sr m^2 V with diffraction effect around 80 fm. In Figure 6.14 an impression is given of a Helium Ion Microscope by ORION. This Helium based ion source could be replaced by a compact ultra-cold Li^+ ion source based on our new ion source concept. Based on a estimate of performance as introduced in section 6.2, we could produce a Li^+ ion beam with a reduced brightness up to $B_r = 4 \times 10^8$ A/sr m^2 V at a current of J =1.5 nA. The parameters are shown in Table 6.5. A simulation of this ion source is done and confirms this result.

Table 6.4: *The numbers used in the estimate of performance of a Lithium-ion source. The laser cooling and trapping parameters are found in [11]*

n	5×10^{18} m^{-3}	T_s	700 K
$\langle v \rangle$	1482 m/s	v_{cap}	3.8 m/s
T_D	142 μK	m	1.12×10^{-26} kg
$\Delta\theta$	3 mrad	L	5 cm
t	33.8 μs	r_i	500 μm
I	3.31 W/cm^2	∇B	0.5 T/m

Figure 6.14: *The ORION Helium ion Microscope from Carl Zeiss SMT delivers a quantum leap in image resolution and material contrast.*

6.7.2 Cs^+ source for ToF-SIMS

Another application using the ultra-cold ion source can be found for the production of heavy ions for time-of-flight secondary ion mass spectroscopy ToF-SIMS. Here cesium (Cs-133) can be used as atomic element. Time-of-Flight Secondary Ion Mass Spectroscopy (ToF-SIMS) is a surface-sensitive spectroscopy that uses a pulsed ion beam to remove molecules from the very outermost surface of the sample. The particles are removed from atomic monolayers on the surface (secondary ions). These particles are then accelerated into a "flight tube" and their mass is determined by measuring the exact time at which they reach the detector (i.e. time-of-flight). A detailed overview of the basics and applications with ToF-SIMS is given in Belu *et al.* [32]. Cesium is already a common element used in these devices. By using a high brightness ion beam the resolution of this technique can be improved. As we did in the previous subsection for the ^{7}Li-source, we calculated an estimate of performance for a ^{133}Cs-source. We found that a cesium ion source with a reduced brightness up to 1.4×10^8 A/sr m^2 V can be produced at a current of J =0.5 nA. Again simulations showed the same value for the reduced brightness of a Cs ion-source.

Table 6.5: *The numbers used in the estimate of performance of a Cesium-ion source. The laser cooling and trapping parameters are found in [11]*

n	2×10^{17} m^{-3}	T_s	317 K
$\langle v \rangle$	229 m/s	v_{cap}	4.4 m/s
T_D	124 μK	m	2.13×10^{-25} kg
$\Delta\theta$	19 mrad	L	5 cm
t	218 μs	r_i	500 μm
I	1.09 W/cm^2	∇B	0.7 T/m

Chapter 7

Conclusions and outlook

7.1 Two-dimensional magneto-optical trap as atomic beam source

The aim of this experimental research project was to investigate the possibilities to use a two-dimensional magneto-optical trap as cold atomic beam source. This atomic beam source can be used to load a 3D-MOT with Rb atoms, which, according to recently published literature, can increase the loading rate and lifetime of the atoms in the 3D-MOT.

Previously, the atoms in the 3D-MOT where loaded from a Rb background vapor. This limits the loading rate and increases the background pressure, which leads to a shorter lifetime. In this case, the maximum loading rate was around 5×10^{7} atoms/s, with a lifetime around 2-3 s. The Rb vapor pressure in the vacuum system was estimated around 8×10^{-10} mbar. Using an atomic beam source from a vapor cell 2D-MOT at low Rb vapor pressures around 5×10^{-8} mbar, we were able to achieve the same loading rate in the 3D-MOT as from the background vapor, but with a lifetime around 6-10 s. We studied the dependence of cooling volume, vapor pressure, laser intensity and magnetic field gradient in the 2D-MOT on the loading rate. Furthermore, we extended a rate equation model based on [13] and [14], that describes the flux generated by a 2D-MOT as function of various system parameters and used it to compare it with our data.

Finally, we expanded our 2D-MOT by adding a push beam. In this case we were able to boost the loading rate in the 3D-MOT to 5×10^{8} atoms/s, with a lifetime around 8-12 s. This is a significant $10\times$ increase in loading rate and $4\times$ increase in lifetime compared to the normal 2D-MOT. The rate equation model used to compare the data from the 2D-MOT was extended to describe the effect of an additional push beam. This new model showed satisfying results. We also built a so-called $2D^{+}$-MOT as described by Dieckmann *et al.* [13], using both a push and retarding beam, but were not able to measure any increase in loading rate. Due to problems with the rubidium vapor in the vapor-cell, we did all experiments at pressures around 5×10^{-8} mbar. From our extended model we predict that increasing the rubidium vapor pressure by one order of magnitude should lead to an equivalent boost in loading rate. Redesigning the system so that higher Rb vapor pressures can be achieved is an important step for future work.

7.2 New type of compact ultra cold Rb^+ ion-source

A new concept for an ultra cold ion source was introduced. This system consists of a rubidium vapor oven and a magneto-optical compressor to produce an ultra-cold and dense atomic beam. By photo-ionizing this atomic beam inside an accelerator structure, an ion beam with very high brightness can be obtained. A quick estimate of the performance was found to exceed state-of-the-art LMI sources in terms of ion beam brightness by far.

To study the performance of such a new ion source more in detail, numerical simulations were done to simulate the particle trajectories of Rb atoms through a magneto-optical compressor. The output of the simulations provided realistic distributions that could be used to calculate reduced brightness and current of this proposed ion source.

Here we found that source temperature, interaction length and magnetic field gradient are important properties to consider when designing such a ion source. At a source temperature of 100^oC and 5 cm of laser collimation a reduced peak brightness around 2×10^5 A/sr m^2 V can be obtained. At the same interaction length and source temperature using both collimation and compression, a reduced peak brightness of 4×10^8 A/sr m^2 V can be obtained with a magnetic field gradient of 0.8 T/m. Recent state-of-the-art LMI sources produced ion beams with reduced brightness up to 10^6 A/sr m^2 V [7]. Based on our estimate and confirmed by the numerical simulations, we found that our new Rb^+ ion source could produce ion beams with a reduced brightness far better than any sources available today.

The next steps in this research would be to design and build such a prototype setup. This work can serve as a guide toward the realization of a new generation of ion sources.

Appendix A

Simulation results of the capture velocity

In this Appendix the simulation results are shown for the dependency of the laser intensity $s_0 = I_{tot}/I_0$, magnetic field gradient ∇B and laser detuning δ/Γ on the capture velocity of the magneto-optical trap. The simulations are done in Matlab.

A.1 Laser intensity dependence

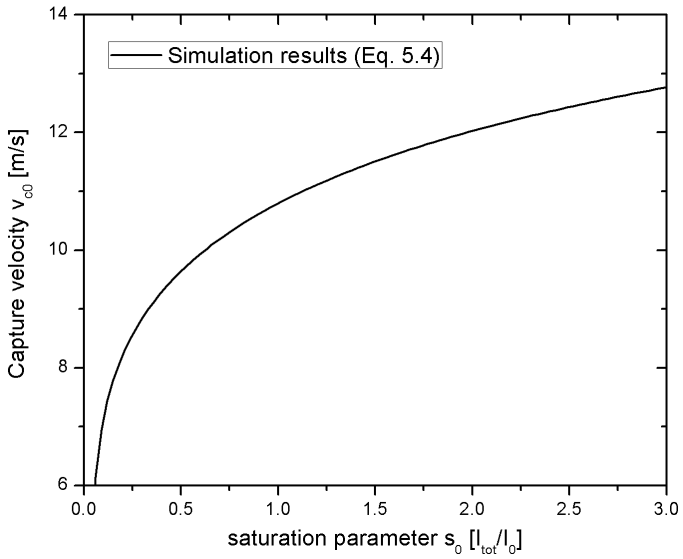

Figure A.1: *Simulation results of the capture velocity as function of (normalized) laser intensity s_0. Here $\delta = -2\Gamma$, $\nabla B = 10$ G/cm and the diameter of the laser beam was $d = 20$ mm.*

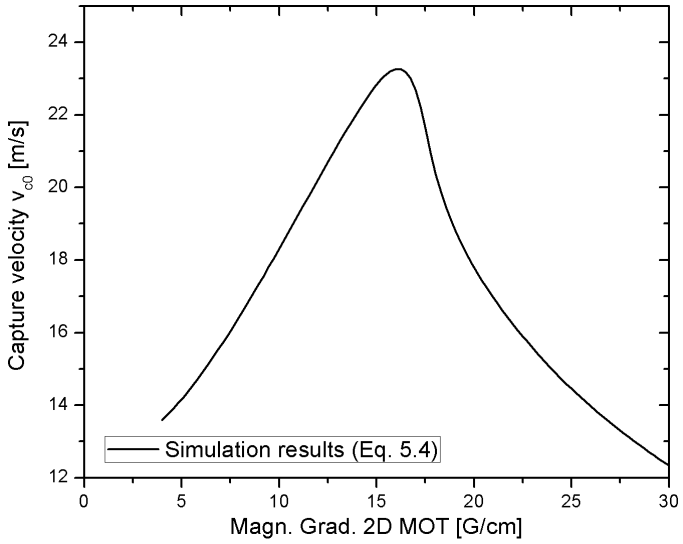

Figure A.2: *Simulation results of the capture velocity as function of the magnetic field gradient in the 2D-MOT. Here* $\delta = -2\Gamma$, $s_0 = 1$ *and the diameter of the laser beam was* $d = 20$ *mm.*

A.2 Magnetic field gradient dependence

A.3 Laser detuning dependence

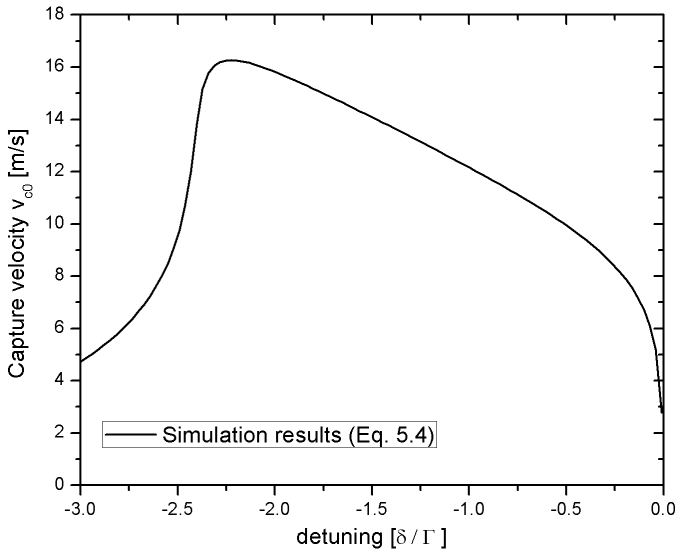

Figure A.3: *Simulation results of the capture velocity as function of (normalized) laser detuning* δ/Γ. *Here* $s_0 = 1$, $\nabla B = 10$ *G/cm and the diameter of the laser beam was* $d = 20$ *mm.*

Appendix B

Matlab code

B.1 Main Program

```
% ============================ close figures ================================
close all;
% ====================== fill initial phase space ==========================

v0 = [10 : 10 : 1000]; theta0 = [-10e-3: 0.1e-3 : 10e-3];
theta0((length(theta0)-1)/2+1)= 5e-6; r = [-5e-4 : 1e-4 : 5e-4];

% ========================= set parameters  ================================

Lbron = 1/10 ;            % Lbron = distance between source and cooling system
L = 1 ;                   % L = cooling length

T = 373;                  % T = temperature  of the source
kB = 1.38e-23;            % kB = Boltzmann constant
m  = 85*1.67e-27;         % m = mass of Rb
A = m./(2*kB*T) ;         % A = m/2kbT

[v0M, theta0M] = meshgrid(v0,theta0); P0 =  cos( theta0M ).*
v0M.^3.*exp(- A.* v0M.^2) ;

%=============================================================================

Yr  = [ ];  Yvr = [ ];  Yvz = [ ];  YP  = [ ];

for i=1: length(r)

    vr0M = v0M.* sin(theta0M) ;
    vz0M = v0M.* cos(theta0M) ;
    r0M  = Lbron.* tan(theta0M) + r(i) ;
    t0M  = L./vz0M  ;
    P0cyl = abs ( P0./v0M );
    Yr  = [Yr ; r0M(:) ];
    Yvr = [Yvr ; vr0M(:) ];
    Yvz = [Yvz ; vz0M(:) ];
    YP  = [YP ; P0cyl(:) ];
```

```
end

Y = [Yr, Yvr, Yvz, YP];

%============= consider only the atoms that pass the aperture ==============

for j=1:length(Y)
    if abs(Y(j,1)) > max(r)
        Y(j,4) = 0;
    end
end

% ================ create 3D figure of initial distribution   ===============

[Me1, xe1, ye1] = mk2dhist(Y(:,1),Y(:,2),Y(:,4) ,200 ,200); [Me2,
xe2, ye2] = mk2dhist(Y(:,1),Y(:,3),abs(Y(:,4)) ,50 ,200); figure;
surfc(ye1,xe1,Me1); xlabel('vr [m/s]'); ylabel('r [m]');
zlabel('P'); figure; surfc(ye2,xe2,Me2); xlabel('vz [m/s]');
ylabel('r [m]'); zlabel('P');

%==========================================================================

x0L  = [Yr, Yvr, Yvz ];

%====================  Calculated moved coordinates  =======================

X1L = transformTrap( x0L, L );
                    % see below for more details about transformTrap
X1L = [r1L , vr1L];

%====================== Calculate RMS velocity & position ==================

v = 0; P = 0; r = 0;

for i=1 : size(X1L,1)
    r = r + X1L(i,1).^2.*Y(i,4).*abs(Y(i,2));
    v = v + X1L(i,2).^2.*Y(i,4).*abs(Y(i,2));
    P = P + Y(i,4).*abs(Y(i,2));
end

v_rms = sqrt(v/P) r_rms = sqrt(r/P)

%========================== Create new 3D histogram ========================

[Me, xe, ye] = mk2dhist((X1L(:,1)),(X1L(:,2)),YP,50,200);
figure;
surfc(ye,xe,Me);
axis([min(ye) max(ye) min(xe) max(xe) 0 max(max(Me))]) %autoscale
xlabel('vr [m/s]'); ylabel('r [m]'); zlabel('P');

%==========================================================================
```

B.2 Functions

transformTrap

```
function X1L = transformTrap(X0L, L)

X1L = [ ]; count =  size(X0L,1); for i=1 : count
    if (i/1000 - floor(i/1000) == 0  )
         display(i/count);
    end;
    r =  X0L(i,1);
    vr = X0L(i,2);
    vz = X0L(i,3);

    tcool = L/vz;       % t = time that atoms interact with MOC

    [T,Y] = ode23(@coolfunTrap,[0 tcool/2 tcool],[r , vr, vz]);
                    % see below for more details about coolfunTrap
    X1Ltemp = Y( length(Y), :); %[r vr vz]

    X1L= [X1L ; X1Ltemp];

end
%=============================================================================
```

coolfunTrap

```
function CoolFunTrap = coolfunTrap(t, x)

%======================== set constants ==================================

hbar = 1.055e-34; k = 2*3.1415 / 780e-9; gamma = 2*3.1415*5.98e6 ; m
= 85 * 1.67e-27; mub = 9.274e-24;

A = 0.5*hbar*k*gamma/m; %0.863e5;        % hbar.k.gamma/2m
C = mub/hbar;           %8.75e10;        % mub/hbar
                        %k = 8.055e6;

%================= set laser cooling parameters ======================

s0 = 1 ;                % s0 = saturation parameter I / Io
delta = -0.5*gamma;     % delta = laser detuning
dB = 0;         % dB = magnetic field gradient in T/m

r = x(1); vr = x(2); vz = x(3);

%========================= differential equation ====================

accel_r = A*s0*(    1/(1+s0+4*((delta - k*vr - C*dB*r)/gamma)^2  ) -
1/(1+s0+4*((delta + k*vr + C*dB*r)/gamma)^2)  ); CoolFunTrap = [ vr;
accel_r; 0 ];
```

```
%=====================================================================
```

calcRMS

```
function [Vrms, Rrms, ratio, Emit, vrms, rrms] = calcRMS2 (X1L, Y,
dia)
       % to calculate the final beam rms values
                     at different beam fractions

v = 0;  P = 0;  r = 0;  vr = 0; rlim = zeros( size(dia) );   vlim =
zeros( size(dia) ); Plim = zeros( size(dia) );   ratio= zeros(
size(dia) ); vrlim= zeros( size(dia) );

for j=1 : length (dia)

    for i=1 : size(X1L,1)

        r = r + X1L(i,1).^2.*Y(i,4).*abs(Y(i,1));
        v = v + X1L(i,2).^2.*Y(i,4).*abs(Y(i,1));
        P = P + Y(i,4).*abs(Y(i,1));
        vr = vr + abs(v*r);

        if ( abs(X1L(i,1)) <  dia(j) )
            rlim(j) = rlim(j) + X1L(i,1).^2.*Y(i,4).*abs(Y(i,1));
            vlim(j) = vlim(j) + X1L(i,2).^2.*Y(i,4).*abs(Y(i,1));
            Plim(j) = Plim(j) + Y(i,4).*abs(Y(i,1));
            vrlim(j) = vrlim(j) + abs(X1L(i,1).*X1L(i,2).*Y(i,4).*Y(i,1));
        end
    end

    vrms = sqrt(v/P);
    rrms = sqrt(r/P);

    Vrms(j) = sqrt(vlim(j)/Plim(j));
    Rrms(j) = sqrt(rlim(j)/Plim(j));
    ratio(j)= Plim(j)/P;
    Emit(j) = sqrt( Vrms(j)^2*Rrms(j)^2 - ( vrlim(j)/Plim(j) )^2 );

    P = 0;
    v = 0;
    r = 0;
end
%=====================================================================
```

Bibliography

[1] J. Cao et al, Proc. Natl. Acad. Sci. USA, **96**, 338 (1999)

[2] R. W. Schoenlein et al, Science, **274**, 236 (1996)

[3] S. Reyntjens, R. Puers *A review of Focused Ion Beam in Microsystem Technology*, J. Micromech. Microeng., **11**, 287300 (2001)

[4] S. Humphries, *Principles of Charged Particles Accelerators*, University of New Mexico (1996)

[5] O.J. Luiten, B.J. Claessens, S.B. van der Geer, M.P. Reijnders, G. Taban, E.J.D. Vredenbregt, *Ultracold electron sources*, (1996)

[6] B.J. Claessens, S.B. van der Geer, G. Taban, E.J.D. Vredenbregt, O.J. Luiten, *Ultracold electron source*, Phys.Rev.Lett. **95**, 164801 (2005).

[7] S.K. Guharay, J. Orloff, and M. Wada, *Ion beam and Their Applications in High-Resolution Probe Formation*, IEEE Transactions on Plasma, Vol 33, **6**, (2005)

[8] B.G. Freinkman, A.V. Eletskii, S.I. Zaitsev, *A proposed laser source of ions for nanotechnology*, Microelectronic Engineering **73-74** (2004) 139-143

[9] M. Reijnders, *Ultracold Electron and Ion Beams*, Master thesis. (Eindhoven University of Technology, 2006).

[10] C.J. Foot, *Atomic Physics*, 2005 Oxford University Press

[11] H.J. Metcalf and P. van der Straten *Laser Cooling and Trapping*, 1999 Springer

[12] R.Wijtvliet, Internal report. (Eindhoven University of Technology, 2004).

[13] K. Dieckmann, R.J.C. Spreeuw, M. Weidemuller, J.T.M. Walraven, *Two-dimensional magneto-optical trap as source of slow atoms*, Phys. Rev. A **58**, 3891 (1998)

[14] J. Schoser, A. Batar, R. Low, V. Schweikhard, A. Grabowski, Yu. B. Ovchinikov, T. Pfau, *Intense source of cold Rb atoms from a pure two-dimensional magneto-optical trap*, Phys. Rev. A, **66**, 023410 (2002)

[15] C. Monroe, W. Swann, H. Robinson, C. Wieman, Phys. Rev. Lett. **65**, 1571 (1990)

[16] Z. T. Lu, K. L. Corwin, M. J. Renn, M.H. Anderson, E. A. Cornell, C.E. Wieman, Phys. Rev. Lett. **77**, 3331 (1996)

[17] S. Chaudhuri, S. Roy, C.S. Unnikrishnan, *Realisation of an intense cold Rb beam on a two-dimensional magneto-optical trap*, Phys. Rev. A **74**, 023406 (2006)

[18] D. Kusters, *Diagnostics of a Rubidium Magento-Optical Trap*,Internal report. (Eindhoven University of Technology, 2006 - **04**).

[19] S.J. Blundell and K.M. Blundell, *Concepts in Thermal Physics*, 2006 Oxford University Press

[20] G. Scoles, *Atomic and Molecular Beam Methodes* Volume I, 1988 Oxford University Press

[21] *Handbook of Chemistry and Physics*, CRC Press, 84th edition, 2003-2004.

[22] E.J.D. Vredenbregt, K.A.H. van Leeuwen, H.C.W. Beijerinck, *Booster for ultrafast loading of atom traps* Opt. Comm. **147**, 375-381 (1998)

[23] B.J. Cleassens, M.P. Reijders, G. Taban, O.J. Luiten , and E.J.D. Vredenbregt, *Physics of Plasmas*, **14**, 093101 (2007)

[24] S. Reyntjens and R. Puers, *A review of focused ion beam applications in microsystem technology*, J. Micromech. Microeng., **11** 287300 (2001)

[25] N. de Jonge, M. Allioux, J.T. Oostveen, K.B.K Teo, and W.I. Milne, *Ion sources*, Phys. Rev. Lett. **94**, 186807 (2005)

[26] D. Aumiler, T. Ban, R. Beuc, G. Pichler, *Simultaneaus determination of the temperature and density of rubidium vapor* Appl. Phys. B **76**, 859-867 (2003)

[27] D. W. Sesko, T. G. Walker, C. E. Wieman, *Behavoir of neutral atoms in a spontaneous force trap*, J. Opt. Soc. Am. B Vol **8**, 5 (1991)

[28] C. Gabbanini, S. Gozzini, A. Lucchesini, *Photoionization cross section measurements in a Rb Vapor cell trap*, Opt. Comm. **141**, 25-28, (1997)

[29] A. di Stefano, Ph. Verkerk, D. Hennequin, *Deterministic instabilities in the magneto-optical trap*, Eur.Phys.J.D. **30**, 243-258 (2004)

[30] T. Walker, D. Sesko, C. Wieman, *Collective behavior of optically trapped neutral atoms*, Phys.Rev.Lett. **64**, 408 (1990)

[31] B.W. Ward, J.A. Notte, N.P. Economou, *Helium ion microscope: A new tool for nanoscale microscopy and metrology*, J. Vac. Sci. Technol. B **24**-6 (2006)

[32] A. M. Belu, D. J. Graham, D.G. Castner, *Time-of-flight secondary ion mass spectroscopy: techniques and applications for the characterization of biomaterial surfaces* Biomaterials **24** 3635-3653 (2003)